Research Square

Preprints are preliminary reports that have not undergone peer review.
They should not be considered conclusive, used to inform clinical practice,
or referenced by the media as validated information.

Heightened B-cell activation and reduced inhibitory signaling are associated with increased susceptibility to immune-related adverse events in cancer patients treated with immune checkpoint inhibitors

Sarah Soussan
Sorbonne Université, Université Paris Cité, Inserm, Centre de Recherche des Cordeliers
Rayan El Kholdi
Sorbonne Université, Université Paris Cité, Inserm, Centre de Recherche des Cordeliers
Lucie Garnier
Sorbonne Université, Université Paris Cité, Inserm, Centre de Recherche des Cordeliers
Lou Lelievre
Sorbonne Université, Université Paris Cité, Inserm, Centre de Recherche des Cordeliers
Sofiene Tifoura
Sorbonne Université, Université Paris Cité, Inserm, Centre de Recherche des Cordeliers
Magali Fradet
College de France
Lea Guyonnet
Institut Curie
Coralie Guerin
Institut Curie
Nicolas Tchitchek
Inserm UMRS 959, Sorbonne Université
Jean-Sébastien Hulot
Université Paris Cité, INSERM, PARCC
Assié Eslami
Assistance Publique - Hôpitaux de Paris
Mariana Mirabel
Institut Médico-Chirurgical Montsouris
Laetitia Meda
Université Paris Cité, Assistance Publique-Hôpitaux de Paris, Cancer institute APHP-nord Paris Cité, INSERM U1342 - Equipe 1 - CNRS EMR8000, Saint Louis Hospital
Pierre-Emmanuel Joubert

Sorbonne Université, Université Paris Cité, Inserm, Centre de Recherche des Cordeliers

Isabelle Cremer

Sorbonne Université, Université Paris Cité, Inserm, Centre de Recherche des Cordeliers

Céleste Lebbé

Université Paris Cité, Assistance Publique-Hôpitaux de Paris, Cancer institute APHP-nord Paris Cité, INSERM U1342 - Equipe 1 - CNRS EMR8000, Saint Louis Hospital

Marie-Agnès Dragon Durey

Sorbonne Université, Université Paris Cité, Inserm, Centre de Recherche des Cordeliers

Sophie Sibéril

sophie.siberil@sorbonne-universite.fr

Sorbonne Université, Université Paris Cité, Inserm, Centre de Recherche des Cordeliers

---

Research Article

Keywords: Immunotherapy in cancer patients, Immune checkpoint inhibitors, Immune-related adverse events, B lymphocytes

Posted Date: September 14th, 2026

DOI: https://doi.org/10.21203/rs.3.rs-10386359/v1

License: This work is licensed under a Creative Commons Attribution 4.0 International License. Read Full License

Additional Declarations: No competing interests reported.

Abstract

Immune checkpoint inhibitors (ICI) targeting CTLA-4 and PD-1 improve cancer outcomes but are frequently associated with breakdown of peripheral tolerance, triggering immune-related adverse events (irAEs). While T-cell mediated mechanisms have been extensively studied, the contribution of B cells in irAE pathogenesis remains underexplored. Here, we performed comprehensive phenotypic, functional, and signaling analyses of peripheral B cells in two independent ICI-treated patient cohorts: a melanoma cohort (PREDIMEL) and a pan-cancer cohort (AMICI). Before treatment initiation, patients who subsequently developed irAEs displayed enrichment of highly activated and differentiated B-cell subsets, including IgD^- memory B cells, activated memory B cells, and plasmablasts depending on cancer type. Beyond these phenotypic alterations, B cells from irAE-prone melanoma patients exhibited intrinsic functional dysregulation, characterized by enhanced BCR-induced signaling through Syk and PLCγ2 phosphorylation and increased antibody secretion upon stimulation. Despite inter-tumor and inter-cohort heterogeneity, irAE-associated B-cell subsets shared a common signature of increased activation and reduced inhibitory receptor expression. Together, these findings identify a pre-existing B-cell state with heightened activation potential and impaired regulation, revealing a functional B-cell predisposition that may contribute to immune toxicity following ICI therapy.

Introduction

By reactivating anti-tumor immunity, immune checkpoint inhibitors (ICI), including anti-CTLA-4 and anti-PD-1 monoclonal antibodies (mAbs), can also disrupt peripheral immune tolerance and induce immune-related adverse events (irAEs), affecting 30–90% of treated patients. IrAEs can involve multiple organs, including the skin, endocrine glands, lungs, gastrointestinal tract, liver, nervous system, kidneys, and heart, and may lead to severe morbidity, long-term organ dysfunction, or permanent discontinuation of ICI therapy [1]. Current management of severe irAEs relies mainly on broad immunosuppression with glucocorticoids, which can cause significant side effects and potentially compromise anti-tumor immunity [2, 3]. Understanding the mechanisms underlying ICI-induced autoimmunity is therefore essential to develop more targeted approaches that preserve therapeutic efficacy.

Most studies investigating irAE pathogenesis have focused on T cells, the primary targets of ICI therapy. Several T-cell-related parameters, including frequencies of memory/helper $CD4^+$ T cells, activated $CD8^+$ T cells, proliferating Ki-67^+ T cells, and inflammatory cytokines/chemokines signatures, have been correlated with irAEs occurrence [1, 4–6]. Additionally, CTLA-4 blockade may further promote autoimmunity by impairing regulatory T-cell function and disrupting peripheral tolerance [7, 8]. In addition, tumor-associated antigen release following effective anti-tumor responses may activate autoreactive T cells recognizing shared tumor and healthy tissue antigens, contributing to tissue damage during irAEs [9, 10].

Beyond T cells, increasing evidence implicates B cells in both ICI efficacy and toxicity. Tumor-infiltrating B cells, particularly those organized within tertiary lymphoid structures (TLS), circulating B-cell subsets,

and T follicular helper (Tfh)-like cells have been associated with clinical responses to ICI [11–13]. Conversely, the frequent detection of autoantibodies in patients developing irAEs suggests that B cells may also contribute to immune-mediated toxicity [14]. Alterations in B-cell receptor (BCR) repertoires, immunoglobulin expression, regulatory B-cell compartments, and expansion of autoreactive $CD21^{low}$ B cells have been reported in patients experiencing ICI-related toxicities, although results remain heterogeneous and sometimes contradictory across studies [15–21]. Genetic evidence linking enhanced B-cell maturation pathways, such as IL-7 signaling, with increased susceptibility to irAEs further supports a role for B-cell dysregulation in this process [22].

However, the precise mechanisms by which B cells contribute to ICI-induced autoimmunity remain poorly understood. Previous studies have mainly focused on global B-cell frequencies, selected subsets, or transcriptional signatures, without comprehensively addressing the activation state and functional competence of individual B-cell populations. Here, we performed an integrated phenotypic and functional characterization of peripheral B cells in two independent ICI-treated patient cohorts, including melanoma and pan-cancer populations. Using high-dimensional spectral flow cytometry, BCR signaling assays, and functional evaluation of antibody production, we identified a shared mechanism linking pre-existing activation of memory and highly differentiated B-cell subsets with susceptibility to irAEs across cancer types.

Materials and methods

Patients and samples

Patients with melanoma were enrolled in the prospective, single-center PREDIMEL clinical trial ("Definition of an Immune Signature Predictive of Anti-PD-1 Antibody in the Treatment of Advanced Melanoma", ClinicalTrials.gov Identifier: NCT02938728) conducted at Saint-Louis Hospital (Paris, France). IrAEs were graded according to ESMO Clinical Practice Guidelines. High-dimensional flow cytometry and B-cell culture experiments were performed in an initial cohort of 37 patients with stage III-IV melanoma (PRED_1, Supplementary Table 1), enrolled between June 15, 2020 and November 22, 2021, and treated with either nivolumab (n = 6) or nivolumab plus ipilimumab (n = 31). A second subcohort of 25 patients (PRED_2, Supplementary Table 2), all receiving combined anti-PD1 and anti-CTLA-4 therapy, was selected according to irAEs severity (grade 1–2, n = 4; grade 3–4, n = 15) for peripheral B-cell phenotyping and BCR signaling analyses.

An independent cohort of 45 patients with various solid tumors (renal, lung, head and neck, bladder, and gastrointestinal cancers) enrolled in the AMICI clinical study ("Adverse Myocardial and Vascular Side Effects of Immune Checkpoint Inhibitors", ClinicalTrials.gov Identifier: NCT04586894) [23] (Supplementary Table 3) was also analyzed by flow cytometry. Serum, plasma, and PBMC were collected using standard procedures and stored until analysis.

All studies were conducted in accordance with the Declaration of Helsinki, Good Clinical Practice, French regulations, and CNIL requirements. The PREDIMEL and AMICI studies were approved by the relevant ethics committees (Comité de Protection des Personnes Ouest V/20.05.28.47707 and CPP Île-de-France IV 2016/28, respectively), and all participants provided written informed consent.

Flow cytometry experiments

Cryopreserved PBMCs were thawed, washed, and stained with antibody cocktails and Live/Dead dye following FcγR blockade (Fcblock, BD). Cells were then fixed with 0.5% paraformaldehyde and acquired on a Sony ID7000 or BD LSR Fortessa flow cytometer.

For the PRED_1 cohort, deep spectral flow cytometry phenotyping was performed using five antibody panels (Supplementary Tables 4 and 5) including canonical markers of B-cell subsets [24]. Additional PBMC samples were stained for IgG and IgA surface expression using a restricted antibody panel (IgA AF-488 ; IgG PE; CD95 PECF594; IgD PE-Cy7 ; CD19 V450 ; CD27 BV510 ; CD21 BV786 ; CD20 BV570 ; CD38 BV605 ; CD24 APC ; CD45 PerCP ; Dump channel: Live Dead IR /CD3 APC-Cy7 /CD14 APC-Cy7) (Supplementary Table 5). For the PRED_2 cohort, a validation panel was applied on PBMC samples (CD19 V450; CD27 BV510; CD38 BV605; CD21 BV786; CD32 FITC; CD45 RB70; CD20 PE; CD95 PECF594; IgD PECy7; CD24 APC; CD11c BUV395; Dump channel: Live Dead IR /CD3 APC-Cy7 /CD14 APC-Cy7) (Supplementary Table 5).

B-cell culture and differentiation into antibody-secreting cells

Cryopreserved PBMCs were thawed, stained with an antibody panel (Supplementary Table 5) allowing the sorting on a FACS Aria Fusion of two B-cell subsets: IgD^- activated memory B cells (IgD^- AMB) ($CD19^+$ $CD3^-$ $CD14^-$ $CD27^+$ IgD^- $CD24^{low/-}$ $CD38^-$ $CD20^+$ $CD21^+$ $CD95^+$) and IgD^- memory B cells (IgD^- MB) ($CD19^+$ $CD3^-$ $CD14^-$ $CD27^+$ IgD^- $CD24^+$ $CD38^-$ $CD20^+$ $CD21^+$). Sorted cells were cultured as previously described on B21 feeder cells expressing human CD40L, BAFF and IL-21 [25], in complete medium supplemented with IL-2 and IL-4 for 32 days. Culture supernatants were collected throughout the culture period, pooled at day 32, clarified by centrifugation, and concentrated using 100-kDa Amicon Ultra centrifugal filters (Merck Millipore) to purify secreted antibodies.

Immunoglobulin quantification

IgG and IgA concentrations in patient sera and B-cell culture supernatants were measured using ELISA kits (IgG Human Uncoated ELISA kit and IgA Human Uncoated ELISA kit, Invitrogen) according to the manufacturer’s instructions.

Phospho-flow cytometry

PBMCs were thawed and stimulated for 10 min at 37°C with increasing concentrations (10–100 µg/mL) of anti-human IgG in Fab'_2 or IgG format (Jackson ImmunoResearch), or left unstimulated. Cells were stained with an extracellular antibody panel (CD45-PerCp; IgD-PE-Cy7; CD19 V450; CD27 BV510; Dump channel: Live Dead IR/CD3 APC-Cy7/CD14 APC-Cy7) (Supplementary Table 5), fixed, permeabilized and then stained with phospho-specific antibodies (p-ZAP70/p-Syk and p-PLCγ2), and acquired on a BD LSR Fortessa flow cytometer.

Analysis of circulating ANA antibodies

Antinuclear antibodies (ANAs) were assessed by indirect immunofluorescence on Hep-2 cells (Euroimmun; RRID:CVCL_1906). Patients were considered ANA-positive for titers ≥ 1:80, and clinically significant ANAs were defined as titers ≥ 1:160. ANA patterns were classified according to the International Consensus on ANA Patterns (ICAP) and grouped as nuclear (speckled, homogeneous, nucleolar, centromere), cytoplasmic, mixed nuclear/cytoplasmic, or negative. Comparisons between $irAEs^+$ and $irAEs^-$ groups were performed using the chi-square (χ^2) test.

Spectral flow cytometry data analysis

For spectral flow cytometry analysis, data were first pre-processed using FlowJo software (RRID:SCR_008520) to isolate singlets, live, $CD45^+CD3^-CD14^-CD19^+$ B cells and to perform compensation corrections (Fig. S1). The resulting FCS files were analyzed using OMIQ software. Dimensionality reduction was performed using the UMAP (Uniform Manifold Approximation and Projection) algorithm (n_neighbors = 20, min_dist = 0.4). Clustering was carried out using the FlowSOM algorithm (RRID:SCR_016899) (10 × 10 grid, k = 20 clusters). The same experimental and analytical workflow was applied to all five panels (Fig. S2). For each cluster within each panel, cluster frequencies (percentage of total B cells) and the mean fluorescence intensity (MFI) of common markers (CD19, CD20, CD27, IgD, CD38, CD24, CD21 and CD11c) were exported for downstream analysis in R. Cross-panel cluster merging was performed using the Hierarchical Density-Based Spatial Clustering of Applications with Noise (HDBSCAN) algorithm using default parameters (minimum cluster size = 2). Clusters derived from independent panels that displayed similar phenotypic profiles and relative abundance were merged (Fig. 1A), while clusters that could not be merged were retained for subsequent analysis. A UMAP visualization of clusters was generated (n_neighbors = 50, min_dist = 0.1) to highlight merged and un-merged clusters (Fig. 1B). Merged and unmerged clusters were annotated using canonical B-cell markers corresponding to established peripheral blood B-cell subsets, including transitional, naive, IgD^+ memory, IgD^- memory, IgD^- activated memory, pre-plasmablast, plasmablast, naive activated, and double negative B cells (34, 35). These annotated populations were referred to as B-cell metaclusters in this study. The relative abundances and phenotypic characteristics of both merged and un-merged clusters, as well as B-cell metaclusters, were analyzed in R. Cluster identities were visualized as heatmaps of the z-scored MFI values of each marker using ComplexHeatmap R package (RRID:SCR_017270) (Fig. 1D). Scatterplots, boxplots, violin plots and bar plots were generated using the ggplot2 package

(RRID:SCR_014601). Principal Component Analysis (PCA) of individual patients was performed based on the relative abundance of B-cell metaclusters using the FactoMineR (RRID:SCR_014602) and Factoextra packages (RRID:SCR_016692).

Conventional flow cytometry data analysis

For the evaluation of surface IgG and IgA expression, flow cytometry data were processed in FlowJo, and the frequencies of IgA^+ and IgG^+ cells were depicted using PRISM software. Phospho-flow cytometry data were processed in FlowJo for supervised analysis of p-Syk^+ and p-$PLC\gamma2^+$ cells in total B cells ($CD19^+$, Live, $CD45^+$, $CD3^-$, $CD14^-$), naive B cells ($CD19^+$, $CD27^-$, IgD^+), or memory B cells ($CD19^+$, $CD27^+$, IgD^-). An unsupervised analysis was also performed with UMAP (n_neighbors = 10, min_dist = 0.4) and FlowSOM algorithms (10 × 10 grid, k = 10 clusters) using OMIQ software. Percentage of clusters among B cells were subsequently analyzed using R as previously described.

Statistical analysis

Unpaired comparisons were carried out using a two-tailed Mann–Whitney–Wilcoxon test (non-parametric test for unpaired data). For comparisons involving more than two independent groups, the Kruskal–Wallis test was applied, followed by Benjamini–Hochberg correction for multiple testing. Paired comparisons were performed using the two-tailed Wilcoxon signed-rank test (non-parametric test for paired data), followed by Bonferroni correction. Pearson's R correlation coefficient was computed using R programming's cor.test function. A p-value < 0.05 was considered significant. Significance levels are reported as follows: ns = not significant; * $p < 0.05$; ** $p < 0.01$; *** $p < 0.001$.

Publicly Available scRNA-seq Data Analysis

Publicly available scRNA-seq data from patients with immune checkpoint inhibitor–associated colitis and controls were explored using the Gene Contrasts web interface (Harvard Medical School; https://villani.mgh.harvard.edu/ircolitis/), based on the dataset published by Thomas et al. [26]. Differential expression statistics were retrieved using the platform's default parameters to compare patients with ICI-associated colitis to controls. Expression of FCGR1A, FCGR1B, FCGR2A, FCGR2B, FCGR3A, and FCGR3B was analyzed, comparing *case* (patients on ICI therapy with immune checkpoint inhibitor–associated colitis) versus *control* (patients on ICI therapy without colitis and healthy controls). Differentially expressed genes were defined by an absolute fold change > 1.5, FDR < 0.05, and expression in > 1% of cells.

Data Availability

The data generated in this study are available upon request to the corresponding author.

Results

Longitudinal high-dimensional profiling identifies baseline expansion of activated IgD $^{-}$ memory B cells in melanoma patients developing irAEs

We performed a longitudinal, high-dimensional analysis of peripheral B-cell subsets in a first cohort of 37 advanced-stage melanoma patients treated with either anti-PD-1 monotherapy or combined anti-PD-1 plus anti-CTLA-4 immune checkpoint blockade (PRED_1 cohort, Supplementary Table 1). Among them, 22 patients developed immune-related adverse events ("irAEs^{+}" group), whereas 15 did not exhibit toxicity ("irAEs^{-}" group). Reported toxicities were predominantly grade 1–2 (77%).

PBMC collected before treatment initiation (Timepoint 1), three weeks after ICI initiation (Timepoint 2) and at the onset of irAEs, were analyzed by spectral flow cytometry using five complementary panels comprising 29 markers, including eight shared B-cell markers (CD11c, CD19, CD20, CD21, CD24, CD27, CD38, and IgD) [24] (Fig. 1A; Supplementary Table 4). Unsupervised FlowSOM clustering combined with UMAP visualization was applied to the entire dataset of gated live CD45^{+}CD19^{+}CD3^{-}CD14^{-} B cells (Supplementary Fig. S1), identifying 20 clusters per panel (Supplementary Fig. S2). Clusters displaying similar canonical marker expression and comparable frequencies across patients were integrated across panels (see Methods), resulting in 26 merged clusters, while 17 phenotypically distinct clusters remained separately annotated (Fig. 1A-C). This integrative approach enabled high-resolution phenotypic characterization of peripheral B-cell heterogeneity by combining complementary marker information across panels (Fig. 1D). The resulting clusters were annotated into nine canonical B-cell metaclusters [transitional, naive, activated naive, double negative, IgD^{+} memory, IgD^{-} memory (IgD^{-}MB), activated IgD^{-} memory (IgD^{-}AMB), pre-plasmablasts, plasmablasts] (Fig. 1A and 1D; Supplementary Table 6; Supplementary Fig. S3A). Peripheral B cells were predominantly naive (approximately 70–76% depending on timepoint), while switched IgD^{-} and unswitched IgD^{+} memory B cells represented the major memory populations (Supplementary Table 7).

We next compared the abundance of B-cell clusters between patients who developed irAEs and those who remained toxicity-free. Before ICI treatment (Timepoint 1), three merged clusters (12, 13, and 19) and one unmerged cluster (P5_03) were significantly enriched in patients who subsequently developed irAEs (Fig. 2A). Three additional clusters showed a similar trend although these differences did not reach statistical significance (P2_16, $p = 0.055$; P4_11, $p = 0.07$; P5_04, $p = 0.055$) (Fig. 2A). Most of these differences were no longer observed three weeks after ICI initiation (Timepoint 2), with the exception of P5_04, which was significantly elevated in irAEs^{+} patients (Fig. 2B). Phenotypic annotation revealed that clusters 12, 19, and P5_03 mapped to the IgD^{-} MB metacluster, whereas cluster 13, as well as P2_16 and P4_11, belonged to the IgD^{-} AMB metacluster. In contrast, P5_04 was classified within the double-negative (CD27^{-}IgD^{-}) B-cell metacluster (Fig. 1D; Supplementary Fig. S3B and S3C). At the metacluster level, irAEs^{+} patients exhibited a higher baseline frequency of IgD^{-}AMB cells and a trend towards increased IgD^{-}MB cells. At Timepoint 2, plasmablasts were significantly increased in irAEs^{+} patients (Fig. 2C and 2D).

Functionally primed IgD $^{-}$ memory B cells characterize irAEs^{+} patients at baseline independently of systemic autoantibody levels

Given the baseline enrichment of IgD^{-}MB and IgD^{-} AMB subsets in irAEs^{+} patients, we next investigated their phenotypic and functional properties across the cohort. IgD^{-} AMB cells exhibited a highly activated phenotype characterized by elevated expression of CD95 and CD80, and low expression of inhibitory receptors, including CD32, CD85j, and LAIR-1 (Fig. 3A; Supplementary Table 8). Their phenotypic proximity to plasmablasts suggested an intermediate differentiation state between conventional IgD^{-}MB cells and antibody-secreting cells (Fig. 3A; Supplementary Table 8; Supplementary Fig. S3A). Both IgD^{-} AMB and IgD^{-} MB subsets contained a higher proportion of IgA^{+} cells compared to IgG^{+} cells (Supplementary Fig. S4A–B), suggesting preferential IgA commitment within switched memory compartments. Following flow cytometry-based sorting (Supplementary Fig. S4C), *in vitro* differentiation into antibody-secreting cells confirmed that both subsets produced more IgA than IgG (Fig. 3B). However, while IgG production was comparable, IgD^{-} AMB cells secreted significantly higher amounts of IgA (Fig. 3B and 3C).

We then asked whether the functional capacity of IgD^{-} memory B-cell subsets differed between irAEs^{+} and irAEs^{-} patients. Strikingly, IgD^{-} MB cells from irAEs^{+} patients produced significantly higher levels of IgG at baseline compared to those from irAEs^{-} patients (Fig. 3D). A similar, although not statistically significant, trend toward increased IgA secretion was observed in both IgD^{-} memory subsets (IgD^{-}MB and IgD^{-} AMB) from irAEs^{+} patients (Fig. 3E).

Despite this enhanced cellular activation state, systemic humoral parameters were not altered. Total serum IgG and IgA concentrations were comparable between groups, although IgG levels increased after treatment in irAEs^{+} patients (Supplementary Fig. S5). Likewise, ANA positivity and staining patterns were similar between groups before (57% vs 58%, $\chi^2 = 0.07$) and after ICI initiation (54% vs 62%, $\chi^2 = 0.16$) (Supplementary Table 9) with no change at irAE onset (54%) and no qualitative shift in staining patterns. Thus, susceptibility to irAEs was associated with a pre-existing pool of activated and functionally primed memory B cells rather than established systemic autoimmunity.

Reduced inhibitory checkpoint expression in circulating B cells from irAEs^{+} melanoma patients

We next investigated whether circulating B cells from irAEs^{+} patients exhibited a broader imbalance between activating and inhibitory signaling pathways (Fig. 3; Supplementary Table 10). Consistent with an overall activated phenotype, increased CD95 expression was observed on activated naive B cells at baseline and on plasmablasts after ICI initiation (Supplementary Table 10). Among inhibitory receptors, LAIR-1 expression was significantly reduced on double-negative B cells at baseline, whereas CD22 expression was increased on IgD^{+} memory B cells at timepoint 2 (Supplementary Table 10).

The most consistent alteration involved the inhibitory Fcγ receptor CD32 (FcγRIIB). At the total B-cell level, CD32 expression tended to be lower in irAEs$^+$ patients before treatment ($p = 0.059$) and became significantly reduced after ICI initiation (Fig. 4A, 4C and 4D). At baseline, CD32 expression was significantly decreased on IgD$^+$ memory, IgD$^-$ MB, pre-plasmablast, and double-negative B-cell subsets, with similar trends in plasmablasts and activated naïve B cells (Fig. 4B). This reduction persisted after treatment in IgD$^+$ memory and IgD$^-$ MB cells (Fig. 4E). Importantly, CD32 expression on total B cells after treatment inversely correlated with the severity grade of the first irAE (Fig. 4F), supporting a link between reduced inhibitory signaling and clinical outcome.

To further investigate Fcγ receptor dysregulation, we analyzed publicly available single-cell multi-omic data from ICI-treated patients with colitis [38]. Although FCGR2B expression did not differ between irAE$^+$ and irAE$^-$ patients in this independent dataset, activating Fcγ receptors (FCGR1A/CD64 and FCGR3A/CD16) were markedly upregulated in colonic myeloid cells from irAEs$^+$ patients (Supplementary Table 11). Together, these findings suggest that an imbalance between inhibitory and activating Fcγ receptor signaling may contribute to irAE pathogenesis.

Enhanced BCR signaling before treatment in memory B cells from patients who developed irAEs

To compare B-cell activation potential between irAEs$^+$ and irAEs$^-$ patients prior to treatment, we analyzed by flow cytometry the phosphorylation of Syk and PLCγ2, two key kinases downstream of BCR signaling (Fig. 5). BCR signaling was triggered using either an Fab'_2 anti-BCR fragment that selectively engages the BCR or a full IgG anti-BCR antibody, that co-engages the BCR and the inhibitory receptor FcγRIIB (CD32), thereby mimicking immune complex-mediated regulation of BCR signaling (Fig. 5A). Both reagents were used at concentrations ranging from 10 to 100 µg/ml.

Because CD32 expression on total B cells was inversely correlated with the severity of the first irAE (Fig. 4F) and the PRED_1 cohort mainly included grade 1/2 toxicities, phosphorylation assays were performed in the independent PRED_2 cohort, enriched in grade 3/4 irAEs (Supplementary Table 2). Kinase phosphorylation was assessed in 22 patients, including 5 with grade 1/2 irAEs, 12 with grade 3/4 irAEs, and 5 without toxicity.

FlowSOM clustering combined with UMAP visualization of CD27, IgD, p-PLCγ2, and p-Syk expression identified ten B-cell clusters, including eight enriched for p-Syk expression (clusters 3 to 10), and two co-expressing p-PLCγ2 and p-Syk (8 and 9) (Fig. 5B). Across stimulation conditions, phosphorylated clusters 3 ,4, 5, 6, 8 and 9 were consistently enriched in irAEs$^+$ patients, whereas non-phosphorylated clusters 1 and 2 predominated in irAEs$^-$ patients (Fig. 5C,D; Supplementary Table 12a). In addition, in irAEs$^+$ patients, the frequencies of p-Syk$^+$/p-PLCγ2$^+$ clusters 8 and 9 in response to 10 and 25 µg/mL IgG positively correlated with clinical toxicity severity (Fig. 5E).

Consistent with these unsupervised analyses, supervised gating revealed a higher proportion of p-PLCγ2$^+$ CD19$^+$CD27$^+$IgD$^-$ memory B cells in irAEs$^+$ patients following IgG stimulation at 10, 25 and 50

µg/mL (Fig. 5F; Supplementary Table 12b). Similarly, p-Syk levels were significantly higher in memory B cells from irAEs$^+$ patients following stimulation with F(ab')$_2$ (25–100 µg/mL) and IgG (10–100µg/ml) (Fig. 5F; Supplementary Table 12b).

Overall, these findings indicate that patients who subsequently developed severe irAEs exhibited heightened BCR-triggered signaling before treatment initiation, particularly within the memory B-cell compartment.

Pan-cancer analysis reveals cancer type-specific B-cell activation profiles associated with irAEs

To determine whether these alterations extended beyond melanoma, we applied the same spectral flow cytometry workflow to a prospective pan-cancer cohort of 45 ICI-treated patients (AMICI cohort; ClinicalTrials.gov Identifier: NCT04586894; Supplementary Table 3) [23].

Pretreatment PBMCs were analyzed using the same pipeline as for the PREDIMEL cohort (Fig. 1), and B-cell metacluster frequencies were compared between irAEs$^+$ and irAEs$^-$ patients.

In the overall AMICI cohort, irAEs$^+$ patients displayed reduced total B-cell frequencies and increased plasmablast abundance, whereas IgD$^-$ AMB frequency were not significantly altered (Fig. 6A). Phenotypic analysis nevertheless revealed increased CD95 expression within IgD$^-$ MB, IgD$^-$ AMB, and pre-plasmablast subsets in irAEs$^+$ patients, particularly in lung cancer patients (Fig. 6B; Supplementary Table 13). IrAEs$^+$ lung cancer patients also exhibited increased expression of CXCR5 (a chemokine receptor commonly associated with germinal center reactions and B-cell follicular homing), across multiple B-cell subsets, including IgD$^-$ MB and IgD$^-$ AMB cells (Fig. 6C; Supplementary Table 13).

To investigate these cancer-specific differences, we compared baseline B-cell landscapes across melanoma (n = 58), renal cancer (n = 21), and lung cancer (n = 15). Principal component analysis (PCA) showed that melanoma and renal cancer patients largely clustered together, whereas a subset of lung cancer patients segregated separately (Fig. 6D). Accordingly, lung cancer patients displayed significantly higher frequencies of activated and highly differentiated B-cell subsets, including IgD$^-$ MB, IgD- AMB, plasmablasts and double-negative B cells, while melanoma and renal cancer patients exhibited larger naïve B-cell compartments (Fig. 6E). These differences may underlie the cancer type–specific B-cell signatures associated with irAEs.

Nevertheless, although the specific B-cell subsets associated with irAEs differed across tumor types, both the AMICI and PREDIMEL cohorts support a shared mechanism in which enhanced baseline activation of memory and highly differentiated B-cell populations predispose patients to develop irAEs following ICI therapy (Fig. 7).

Discussion

In this study, we performed an in-depth flow cytometry profiling of peripheral B-cell subsets in cancer patients before and after ICI treatment. Our results reveal significant baseline differences between patients who subsequently developed irAEs and those who did not, notably in the composition, activation status, and inhibitory receptor expression of B cells.

In melanoma patients, we identified a higher proportion of clusters belonging to IgD^- MB cells and IgD^- AMB cells at baseline. The phenotype of IgD^- AMB cells closely resembles the $CD95^+$ memory B-cell subset described by Glass et al. [24], representing an intermediate differentiation state between conventional memory B cells and plasmablasts, consistent with previous reports supporting their propensity to differentiate into ASC [27]. Compared with IgD^- MB subset, IgD^- AMB cells produced more IgA and displayed activated phenotype characterized by high CD80 and CD95 expression, together with reduced expression of inhibitory receptors including CD32 (FcγRIIB), CD85j, and LAIR-1. Although CD95 (Fas) is classically associated with apoptosis, accumulating evidence indicates that it can also promote B-cell activation and differentiation depending on the context known [28]. In particular, the soluble form of CD95L (sFasL) enhances the differentiation of memory B cells into ASCs [29] and elevated levels of sFasL have been reported in several autoimmune diseases [30–32]. Moreover, $CD95^+$ memory B-cell populations have been reported across several autoimmune diseases, where they correlate with disease activity and autoantibody production [33–35]. These observations support a potential role for Fas/FasL signaling in irAE pathogenesis by promoting B-cell activation and differentiation.

Further supporting an intrinsically heightened B-cell activation state in $irAEs^+$ patients, we observed significantly reduced expression of the inhibitory FcγRIIB receptor (CD32) across multiple B-cell subsets, including IgD^+ and IgD^- memory B cells, double-negative B cells, and pre-plasmablasts, both at baseline and after treatment. Moreover, FcγRIIB expression after ICI initiation negatively correlated with irAE severity. FcγRIIB is a key regulator of peripheral tolerance that dampens B-cell receptor signaling [36], and its reduced expression or genetic variants have been associated with autoimmune diseases, particularly SLE [36]. These findings raise the possibility that FcγRIIB polymorphisms could predispose cancer patients to irAEs, a hypothesis that warrants investigation in larger cohorts. To further explore Fcγ receptor involvement, we analyzed publicly available single-cell multi-omic data from ICI-treated patients with colitis [26]. Although FCGR2B expression did not differ between $irAEs^+$ and $irAEs^-$ patients, activating Fcγ receptors (FCGR1A/CD64 and FCGR3A/CD16) were markedly upregulated in colonic myeloid cells from $irAEs^+$ patients. Together, these findings suggest that an imbalance between activating and inhibitory Fcγ receptor signaling across immune cell populations may contribute to irAE pathogenesis.

Reduced expression of the inhibitory FcγRIIB receptor together with the enhanced activation status of B cells in $irAEs^+$ patients suggests increased B-cell functional activity. Consistent with this, IgD^- MB cells isolated from $irAEs^+$ patients produced significantly more IgG in vitro than those from $irAEs^-$ patients. Memory B cells from $irAEs^+$ patients also exhibited stronger BCR-induced signaling, with increased phosphorylation of Syk and/or PLCγ2 following stimulation with either Fab'2 or whole IgG anti-BCR antibodies. Supporting this mechanism, a recent germline genetic study of melanoma patients treated

with ipilimumab identified a Syk-upregulating variant (rs7036417) associated with high-grade irAEs, further implicating enhanced BCR signaling in irAE susceptibility [37].

Taken together, these results indicate that the peripheral B-cell compartment of irAEs^{+} patients is more responsive, less tightly regulated, and more prone to activation, likely contributing to pathogenic events during ICI therapy (Fig. 7). Importantly, these alterations were already detectable before ICI initiation, suggesting that some patients harbor pre-existing immune abnormalities predisposing them to irAEs. This differs from the study by Das et al. [19], which identified post-treatment expansions of CD21^{low} B cells and plasmablasts, possibly reflecting differences in analytical approaches (unsupervised clustering *vs*. manual gating) or cohort characteristics.

Similar alterations were observed in the pan-cancer AMICI cohort, although the predominant B-cell subsets differed (IgD^{-} MB and IgD^{-} AMB cells in PREDIMEL, versus plasmablasts in AMICI), potentially owing to differences in tumor types, treatment regiments and/or baseline immune composition. In addition, systematic cardiac monitoring in AMICI enabled the detection of both clinical and subclinical cardiovascular irAEs potentially underreported on other cohorts [23]. However, it should be noted that these events consisted mainly of atrial fibrillation and worsening pre-existing heart failure rather than confirmed ICI-related myocarditis, and the frequent use of concomitant cardiotoxic therapies limits causal attribution to ICIs.

In summary, our findings support a broader role for B cells in irAE pathogenesis by identifying a pre-existing B-cell activation state associated with susceptibility to toxicity. We propose that this primed B-cell compartment synergizes with ICI-reinvigorated T cells through antibody production, antigen presentation, and B–T cell crosstalk. The increased CXCR5 expression observed across B-cell subsets in lung cancer patients, together with previous studies reporting the implication of circulating T follicular helper cells in irAEs [13, 38, 39], points to the CXCL13/CXCR5 axis and tertiary lymphoid structures as potential hubs coordinating these pathogenic interactions. Further elucidation of B cell–mediated mechanisms across tumor and peripheral compartments may enable patient stratification, the identification of predictive biomarkers, and the development of strategies to mitigate immune toxicity while preserving anti-tumor efficacy.

Declarations

Ethics approval and consent to participate

All studies were conducted in accordance with the Declaration of Helsinki, Good Clinical Practice, French regulations, and CNIL requirements. The PREDIMEL and AMICI studies were approved by the relevant ethics committees (Comité de Protection des Personnes Ouest V/20.05.28.47707 and CPP Île-de-France IV 2016/28, respectively), and all participants provided written informed consent.

Authors' Disclosures

S. Sibéril reports research funding from Sanofi, outside the submitted work. C. Lebbé reports payment or honoraria for lectures, presentations, speakers bureaus, manuscript writing, or educational events from Bristol-Myers Squibb, Merck Sharp & Dohme, Pierre Fabre, Erasca, and Immunocore. She also reports support for attending meetings and/or travel from Bristol-Myers Squibb, Merck Sharp & Dohme, and Pierre Fabre, all outside the submitted work. J.-S. Hulot reports that Assistance Publique–Hôpitaux de Paris (AP-HP), his employing institution, has received research grants from Pliant Therapeutics and Sanofi. He has also received speaker, advisory board, or consultancy fees from Alnylam, Amgen, AstraZeneca, Bayer, Novartis, and Novo Nordisk, all unrelated to the present work. R. El-Kholdi reports research funding from Sanofi and holds stock or stock options in Sanofi, outside the submitted work. All other authors declare no conflicts of interest.

Authors contribution

S. Soussan: conceptualization, investigation, formal analysis, data curation, validation, visualization, writing–original draft. **R. El Kholdi:** investigation, formal analysis, data curation, validation. **L. Garnier:** investigation, formal analysis, data curation, validation. **L. Lelievre:** investigation, formal analysis, data curation, validation. **S. Tifoura:** investigation, formal analysis, data curation, validation. **M. Fradet:** methodology, investigation, formal analysis, data curation. **L. Guyonnet:** methodology, investigation, formal analysis, data curation. **C. Guerin:** methodology, investigation, formal analysis, data curation. **N. Tchitchek:** methodology, formal analysis, data curation, writing–review & editing. **J.S. Hulot:** conceptualization, resources (establishment and maintenance of patient cohorts; collection of patient samples and clinical data; principal investigator of clinical trials), data curation (management and organization of clinical datasets), formal analysis, writing–review & editing. **A. Eslami:** resources (establishment and maintenance of patient cohorts; collection of patient samples and clinical data), data curation (management and organization of clinical datasets). **M. Mirabel:** conceptualization, resources (establishment and maintenance of patient cohorts; collection of patient samples and clinical data; principal investigator of clinical trials), data curation (management and organization of clinical datasets), formal analysis, writing–review & editing. **L. da Meda:** data curation (management and organization of clinical datasets), project administration (coordination and regulatory oversight). **P.E. Joubert:** conceptualization, writing–review & editing. **I. Cremer:** conceptualization, writing–review & editing. **C. Lebbé:** conceptualization, resources (establishment and maintenance of patient cohorts; collection of patient samples and clinical data; principal investigator of clinical trials), data curation (management and organization of clinical datasets), formal analysis, writing–review & editing. **M.A. Dragon-Durey:** conceptualization, methodology, investigation, formal analysis, data curation, validation, writing–original draft. **S. Sibéril:** conceptualization, formal analysis, data curation, validation, visualization, resources, supervision, project administration, funding acquisition, writing–original draft, writing–review & editing.

Acknowledgments

The authors would like to thank the patients and their families. This work was supported by research funding from the association “Ligue Nationale contre le cancer” and from INCA (Institut National du

Cancer). S. Soussan was supported by a PhD fellowship from the “Ministère de l’enseignement supérieur et de la recherche“.

References

1. Suijkerbuijk KPM, van Eijs MJM, van Wijk F, Eggermont AMM (2024) Clinical and translational attributes of immune-related adverse events. Nat Cancer 5:557–571. https://doi.org/10.1038/s43018-024-00730-3
2. Pufall MA (2015) Glucocorticoids and cancer. Adv Exp Med Biol 872:315–333. https://doi.org/10.1007/978-1-4939-2895-8_14
3. Bar-Hai N, Ben-Betzalel G, Stoff R, Grynberg S, Schachter J, Shapira-Frommer R, Asher N (2023) Better late than never: the impact of steroidal treatment on the outcome of melanoma patients treated with immunotherapy. Cancers (Basel) 15:3041. https://doi.org/10.3390/cancers15113041
4. Nuñez NG, Berner F, Friebel E et al (2023) Immune signatures predict development of autoimmune toxicity in patients with cancer treated with immune checkpoint inhibitors. Med (N Y) 4:113–129.e7. https://doi.org/10.1016/j.medj.2022.12.007
5. Bukhari S, Henick BS, Winchester RJ et al (2023) Single-cell RNA sequencing reveals distinct T cell populations in immune-related adverse events of checkpoint inhibitors. Cell Rep Med 4:100868. https://doi.org/10.1016/j.xcrm.2022.100868
6. Lucas MW, Burton EM, Dimitriadis P, Huang AC, Long GV, Mitchell TC, Amaria RN, Blank CU (2026) Immune signature-based uncoupling of checkpoint inhibitor efficacy and toxicity. Immunity 59:29–33.e2. https://doi.org/10.1016/j.immuni.2025.11.021
7. Romano E, Kusio-Kobialka M, Foukas PG et al (2015) Ipilimumab-dependent cell-mediated cytotoxicity of regulatory T cells ex vivo by nonclassical monocytes in melanoma patients. Proc Natl Acad Sci USA 112:6140–6145. https://doi.org/10.1073/pnas.1417320112
8. Selby MJ, Engelhardt JJ, Quigley M et al (2013) Anti-CTLA-4 antibodies of IgG2a isotype enhance antitumor activity through reduction of intratumoral regulatory T cells. Cancer Immunol Res 1:32–42. https://doi.org/10.1158/2326-6066.CIR-13-0013
9. Berner F, Bomze D, Diem S et al (2019) Association of checkpoint inhibitor-induced toxic effects with shared cancer and tissue antigens in non-small cell lung cancer. JAMA Oncol 5:1043–1047. https://doi.org/10.1001/jamaoncol.2019.0402
10. Johnson DB, Balko JM, Compton ML et al (2016) Fulminant myocarditis with combination immune checkpoint blockade. N Engl J Med 375:1749–1755. https://doi.org/10.1056/NEJMoa1609214
11. Meylan M, Petitprez F, Becht E et al (2022) Tertiary lymphoid structures generate and propagate anti-tumor antibody-producing plasma cells in renal cell cancer. Immunity 55:527–541.e5. https://doi.org/10.1016/j.immuni.2022.02.001
12. Carril-Ajuria L, Desnoyer A, Meylan M et al (2022) Baseline circulating unswitched memory B cells and B-cell-related soluble factors are associated with overall survival in patients with clear cell renal

cell carcinoma treated with nivolumab within the NIVOREN GETUG-AFU 26 study. J Immunother Cancer 10:e004885. https://doi.org/10.1136/jitc-2022-004885

13. Gutiérrez-Melo N, Baumjohann D (2023) T follicular helper cells in cancer. Trends Cancer 9:309–325. https://doi.org/10.1016/j.trecan.2022.12.007
14. Ghosh N, Chan KK, Jivanelli B, Bass AR (2022) Autoantibodies in patients with immune-related adverse events from checkpoint inhibitors: a systematic literature review. J Clin Rheumatol 28:e498–e505. https://doi.org/10.1097/RHU.0000000000001777
15. Nakahara Y, Matsutani T, Igarashi Y et al (2021) Clinical significance of peripheral TCR and BCR repertoire diversity in EGFR/ALK wild-type NSCLC treated with anti-PD-1 antibody. Cancer Immunol Immunother 70:2881–2892. https://doi.org/10.1007/s00262-021-02900-z
16. Shahabi V, Berman D, Chasalow SD et al (2013) Gene expression profiling of whole blood in ipilimumab-treated patients for identification of potential biomarkers of immune-related gastrointestinal adverse events. J Transl Med 11:75. https://doi.org/10.1186/1479-5876-11-75
17. Patel AJ, Willsmore ZN, Khan N et al (2022) Regulatory B cell repertoire defects predispose lung cancer patients to immune-related toxicity following checkpoint blockade. Nat Commun 13:3148. https://doi.org/10.1038/s41467-022-30863-x
18. Willsmore ZN, Booth L, Patel A et al (2025) Circulating immunoregulatory B cell and autoreactive antibody profiles predict lack of toxicity to anti-PD-1 checkpoint inhibitor treatment in advanced melanoma. J Immunother Cancer 13:e011682. https://doi.org/10.1136/jitc-2025-011682
19. Das R, Bar N, Ferreira M et al (2018) Early B cell changes predict autoimmunity following combination immune checkpoint blockade. J Clin Invest 128:715–720. https://doi.org/10.1172/JCI96798
20. Nishimura K, Konishi T, Ochi T et al (2022) CD21lo B cells could be a potential predictor of immune-related adverse events in renal cell carcinoma. J Pers Med 12:888. https://doi.org/10.3390/jpm12060888
21. van Eijs MJM, Verheijden RJ, van der Wees SA et al (2023) Toxicity-specific peripheral blood T and B cell dynamics in anti-PD-1 and combined immune checkpoint inhibition. Cancer Immunol Immunother 72:4049–4064. https://doi.org/10.1007/s00262-023-03541-0
22. Taylor CA, Watson RA, Tong O et al (2022) IL7 genetic variation and toxicity to immune checkpoint blockade in patients with melanoma. Nat Med 28:2592–2600. https://doi.org/10.1038/s41591-022-02095-5
23. Mirabel M, Eslami A, Thibault C et al (2024) Adverse myocardial and vascular side effects of immune checkpoint inhibitors: a prospective multimodal cardiovascular assessment. Clin Res Cardiol 113:1263–1273. https://doi.org/10.1007/s00392-024-02462-x
24. Glass DR, Tsai AG, Oliveria JP et al (2020) An integrated multi-omic single-cell atlas of human B cell identity. Immunity 53:217–232.e5. https://doi.org/10.1016/j.immuni.2020.06.013
25. Chappert P, Huetz F, Espinasse MA et al (2022) Human anti-smallpox long-lived memory B cells are defined by dynamic interactions in the splenic niche and long-lasting germinal center imprinting.

Immunity 55:1872–1890.e9. https://doi.org/10.1016/j.immuni.2022.08.019

26. Thomas MF, Slowikowski K, Manakongtreecheep K et al (2024) Single-cell transcriptomic analyses reveal distinct immune cell contributions to epithelial barrier dysfunction in checkpoint inhibitor colitis. Nat Med 30:1349–1362. https://doi.org/10.1038/s41591-024-02895-x
27. McGrath JJC, Li L, Wilson PC (2022) Memory B cell diversity: insights for optimized vaccine design. Trends Immunol 43:343–354. https://doi.org/10.1016/j.it.2022.03.005
28. Guégan JP, Legembre P (2018) Nonapoptotic functions of Fas/CD95 in the immune response. FEBS J 285:809–827. https://doi.org/10.1111/febs.14292
29. van Asten SD, Unger PP, Marsman C et al (2021) Soluble FAS ligand enhances suboptimal CD40L/IL-21-mediated human memory B cell differentiation into antibody-secreting cells. J Immunol 207:449–458. https://doi.org/10.4049/jimmunol.2001390
30. Vincent FB, Kandane-Rathnayake R, Koelmeyer R et al (2020) Associations of serum soluble Fas and Fas ligand (FasL) with outcomes in systemic lupus erythematosus. Lupus Sci Med 7:e000375. https://doi.org/10.1136/lupus-2019-000375
31. Nakamura H, Kawakami A, Izumi M et al (2005) Detection of the soluble form of Fas ligand (sFasL) and sFas in the saliva from patients with Sjögren's syndrome. Clin Exp Rheumatol 23:915. PMID: 16396719
32. Hashimoto H, Tanaka M, Suda T et al (1998) Soluble Fas ligand in the joints of patients with rheumatoid arthritis and osteoarthritis. Arthritis Rheum 41:657–662. https://doi.org/10.1002/1529-0131(199804)41:4<657::AID-ART12>3.0.CO;2-N
33. Adlowitz DG, Barnard J, Biear JN et al (2015) Expansion of activated peripheral blood memory B cells in rheumatoid arthritis, impact of B cell depletion therapy, and biomarkers of response. PLoS One 10:e0128269. https://doi.org/10.1371/journal.pone.0128269
34. Jacobi AM, Reiter K, Mackay M et al (2008) Activated memory B cell subsets correlate with disease activity in systemic lupus erythematosus: delineation by expression of CD27, IgD, and CD95. Arthritis Rheum 58:1762–1773. https://doi.org/10.1002/art.23498
35. Simon D, Balogh P, Erdő-Bonyár S et al (2021) Increased frequency of activated switched memory B cells and its association with the presence of pulmonary fibrosis in diffuse cutaneous systemic sclerosis patients. Front Immunol 12:686483. https://doi.org/10.3389/fimmu.2021.686483
36. Smith KGC, Clatworthy MR (2010) FcγRIIB in autoimmunity and infection: evolutionary and therapeutic implications. Nat Rev Immunol 10:328–343. https://doi.org/10.1038/nri2762
37. Ferguson R, Chat V, Morales L et al (2023) Germline immunomodulatory expression quantitative trait loci (ieQTLs) associated with immune-related toxicity from checkpoint inhibition. Eur J Cancer 189:112923. https://doi.org/10.1016/j.ejca.2023.05.011
38. Wang Y, Zhang Z, Xie T et al (2025) Baseline profile peripheral Tfh cells predict immune-related adverse events in immune checkpoint inhibitor therapy of gastrointestinal cancer. Front Immunol 16:1559275. https://doi.org/10.3389/fimmu.2025.1559275

39. Huang NL, Ortega JG, Kimbrell K et al (2025) Polyfunctional T follicular helper cells drive checkpoint-inhibitor diabetes and are targeted by JAK inhibitor therapy. JCI Insight 10:e188843. https://doi.org/10.1172/jci.insight.188843

Figures

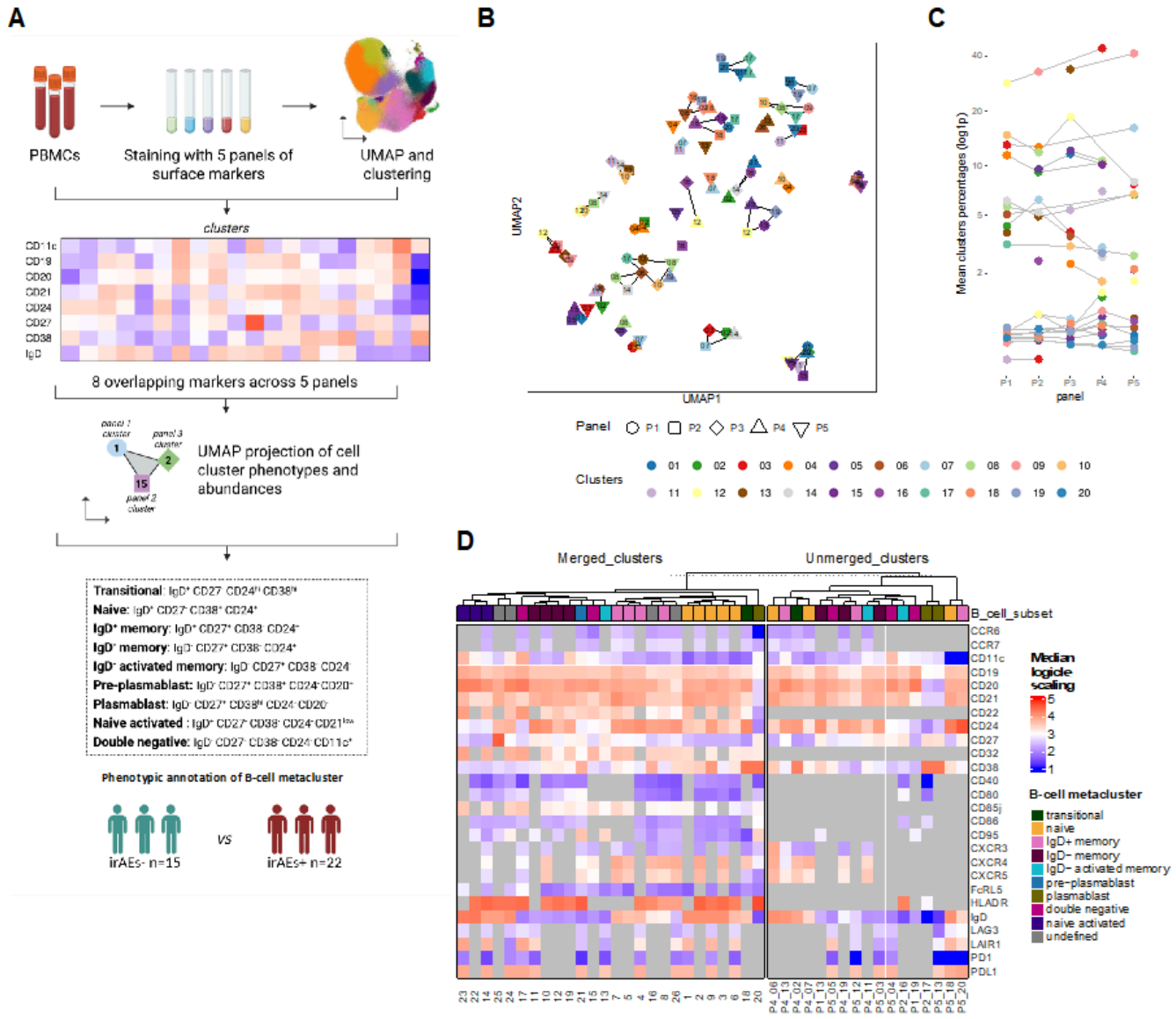


Figure 1

Phenotyping of peripheral B-cell subsets in PRED_1 melanoma patients. A, Graphical overview of the experimental workflow and analysis pipeline used to phenotype peripheral B-cell subsets in PRED_1 cohort (n=37; irAEs$^-$ n=15; irAEs$^+$ n=22). PBMCs were collected before ICI initiation, 3 weeks after the

first cycle of ICI and at irAE onset. Phenotypic characterization of B lymphocytes was performed using five antibody panels analyzed by spectral flow cytometry. An unsupervised analysis of flow cytometry data from all PRED_1 samples enabled the identification of B-cell clusters within each panel. A merging algorithm, based on similarities in the expression of eight overlapping markers across panels and on the relative abundance of clusters among B cells, was applied to merge shared B-cell clusters across panels. Both merged and unmerged clusters were assigned to B-cell metaclusters defined by canonical B-cell markers. Patients who developed irAEs and those who did not were compared at multiple timepoints following ICI initiation. *Created with Biorender.com.* **B**, UMAP visualization of panel-specific clusters obtained in each antibody panel. The UMAP was generated using the cluster frequencies and mean marker expression values per cluster across samples. Panels are indicated by shapes and clusters are numbered from 1 to 20. **C**, Mean abundance of panel-specific clusters among total B cells in PRED_1 samples. (**B**, **C**) Merged clusters are connected by lines, whereas unmerged clusters are shown individually. **D**, Heatmap representation of merged and unmerged cluster phenotypes [mean fluorescence intensity (MFI) of 26 markers; logicle transformation]. A color-coded bar above the heatmap represents the annotation of merged and unmerged clusters into nine B-cell metaclusters Clusters that could not be classified were labeled “undefined”. Detailed data processing is described in the Method section.

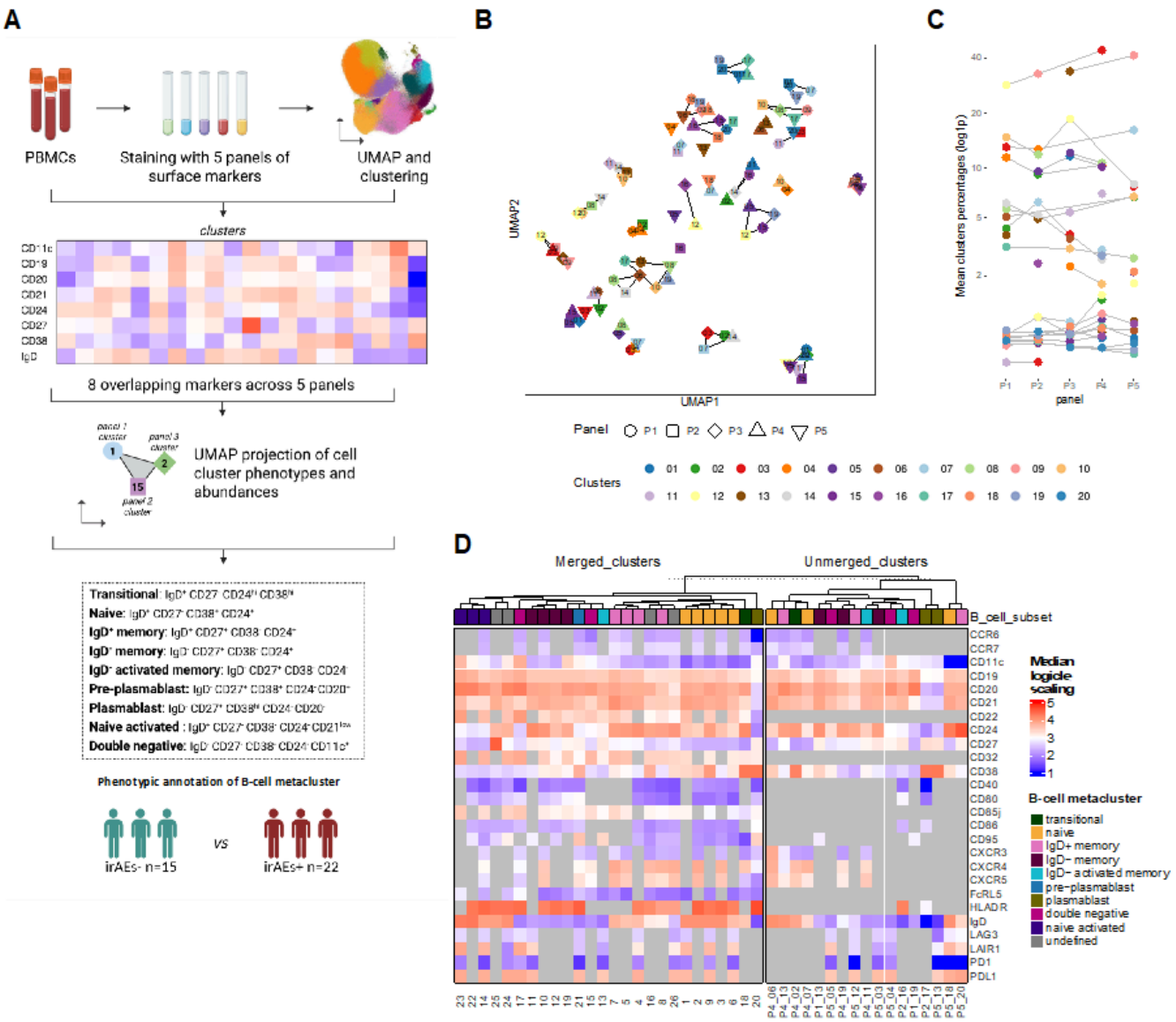


Figure 1

Phenotyping of peripheral B-cell subsets in PRED_1 melanoma patients. A, Graphical overview of the experimental workflow and analysis pipeline used to phenotype peripheral B-cell subsets in PRED_1 cohort (n=37; irAEs$^-$ n=15; irAEs$^+$ n=22). PBMCs were collected before ICI initiation, 3 weeks after the first cycle of ICI and at irAE onset. Phenotypic characterization of B lymphocytes was performed using five antibody panels analyzed by spectral flow cytometry. An unsupervised analysis of flow cytometry data from all PRED_1 samples enabled the identification of B-cell clusters within each panel. A merging algorithm, based on similarities in the expression of eight overlapping markers across panels and on the relative abundance of clusters among B cells, was applied to merge shared B-cell clusters across panels. Both merged and unmerged clusters were assigned to B-cell metaclusters defined by canonical B-cell

markers. Patients who developed irAEs and those who did not were compared at multiple timepoints following ICI initiation. *Created with Biorender.com.* **B**, UMAP visualization of panel-specific clusters obtained in each antibody panel. The UMAP was generated using the cluster frequencies and mean marker expression values per cluster across samples. Panels are indicated by shapes and clusters are numbered from 1 to 20. **C**, Mean abundance of panel-specific clusters among total B cells in PRED_1 samples. (**B**, **C**) Merged clusters are connected by lines, whereas unmerged clusters are shown individually. **D**, Heatmap representation of merged and unmerged cluster phenotypes [mean fluorescence intensity (MFI) of 26 markers; logicle transformation]. A color-coded bar above the heatmap represents the annotation of merged and unmerged clusters into nine B-cell metaclusters Clusters that could not be classified were labeled “undefined”. Detailed data processing is described in the Method section.

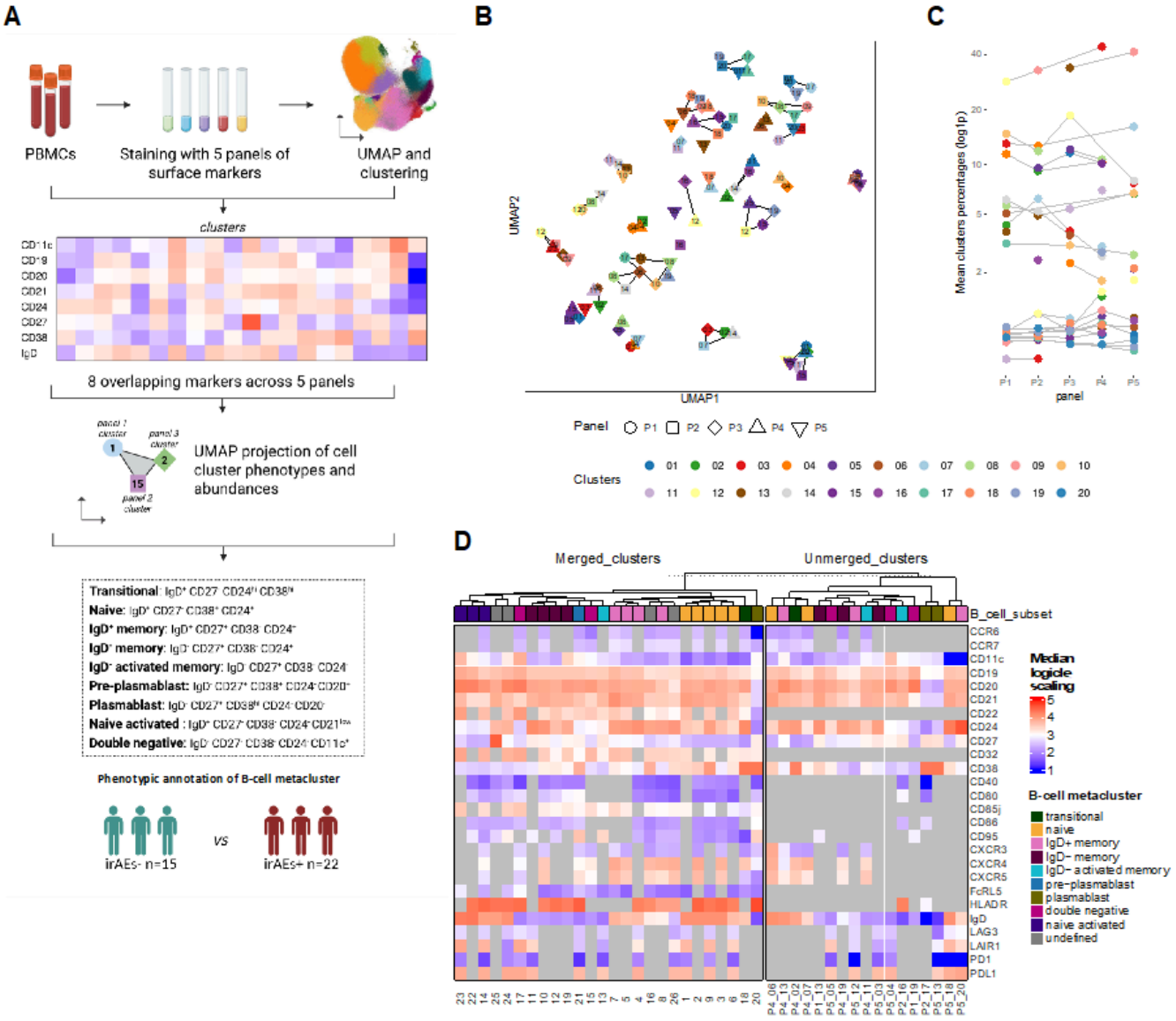


Figure 1

Phenotyping of peripheral B-cell subsets in PRED_1 melanoma patients. A, Graphical overview of the experimental workflow and analysis pipeline used to phenotype peripheral B-cell subsets in PRED_1 cohort (n=37; irAEs^{-} n=15; irAEs^{+} n=22). PBMCs were collected before ICI initiation, 3 weeks after the first cycle of ICI and at irAE onset. Phenotypic characterization of B lymphocytes was performed using five antibody panels analyzed by spectral flow cytometry. An unsupervised analysis of flow cytometry data from all PRED_1 samples enabled the identification of B-cell clusters within each panel. A merging algorithm, based on similarities in the expression of eight overlapping markers across panels and on the relative abundance of clusters among B cells, was applied to merge shared B-cell clusters across panels. Both merged and unmerged clusters were assigned to B-cell metaclusters defined by canonical B-cell markers. Patients who developed irAEs and those who did not were compared at multiple timepoints following ICI initiation. *Created with Biorender.com.* **B**, UMAP visualization of panel-specific clusters obtained in each antibody panel. The UMAP was generated using the cluster frequencies and mean marker expression values per cluster across samples. Panels are indicated by shapes and clusters are numbered from 1 to 20. **C**, Mean abundance of panel-specific clusters among total B cells in PRED_1 samples. (**B**, **C**) Merged clusters are connected by lines, whereas unmerged clusters are shown individually. **D**, Heatmap representation of merged and unmerged cluster phenotypes [mean fluorescence intensity (MFI) of 26 markers; logicle transformation]. A color-coded bar above the heatmap represents the annotation of merged and unmerged clusters into nine B-cell metaclusters Clusters that could not be classified were labeled “undefined”. Detailed data processing is described in the Method section.

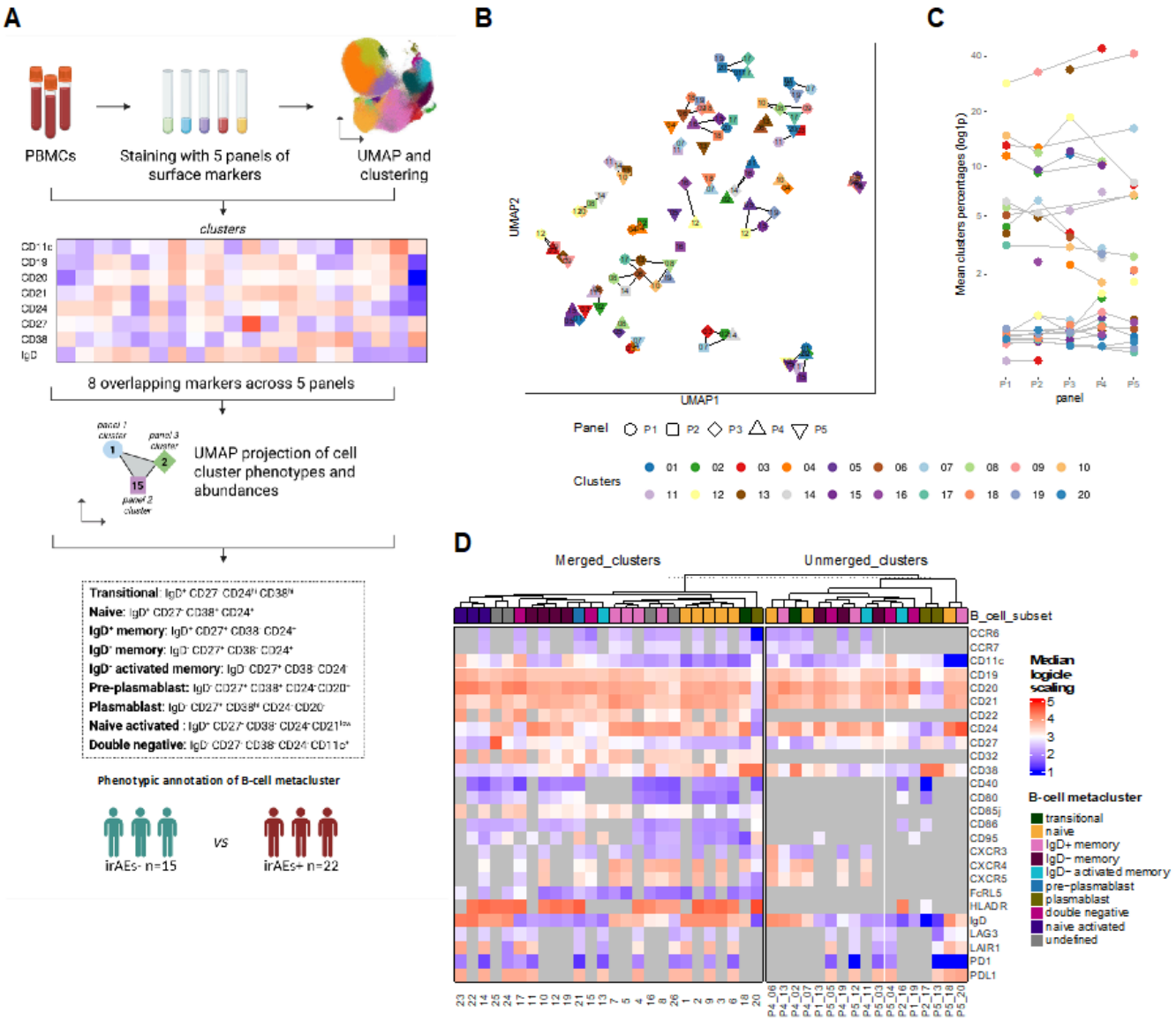


Figure 1

Phenotyping of peripheral B-cell subsets in PRED_1 melanoma patients. A, Graphical overview of the experimental workflow and analysis pipeline used to phenotype peripheral B-cell subsets in PRED_1 cohort (n=37; irAEs$^-$ n=15; irAEs$^+$ n=22). PBMCs were collected before ICI initiation, 3 weeks after the first cycle of ICI and at irAE onset. Phenotypic characterization of B lymphocytes was performed using five antibody panels analyzed by spectral flow cytometry. An unsupervised analysis of flow cytometry data from all PRED_1 samples enabled the identification of B-cell clusters within each panel. A merging algorithm, based on similarities in the expression of eight overlapping markers across panels and on the relative abundance of clusters among B cells, was applied to merge shared B-cell clusters across panels. Both merged and unmerged clusters were assigned to B-cell metaclusters defined by canonical B-cell

markers. Patients who developed irAEs and those who did not were compared at multiple timepoints following ICI initiation. *Created with Biorender.com.* **B**, UMAP visualization of panel-specific clusters obtained in each antibody panel. The UMAP was generated using the cluster frequencies and mean marker expression values per cluster across samples. Panels are indicated by shapes and clusters are numbered from 1 to 20. **C**, Mean abundance of panel-specific clusters among total B cells in PRED_1 samples. (**B**, **C**) Merged clusters are connected by lines, whereas unmerged clusters are shown individually. **D**, Heatmap representation of merged and unmerged cluster phenotypes [mean fluorescence intensity (MFI) of 26 markers; logicle transformation]. A color-coded bar above the heatmap represents the annotation of merged and unmerged clusters into nine B-cell metaclusters Clusters that could not be classified were labeled “undefined”. Detailed data processing is described in the Method section.

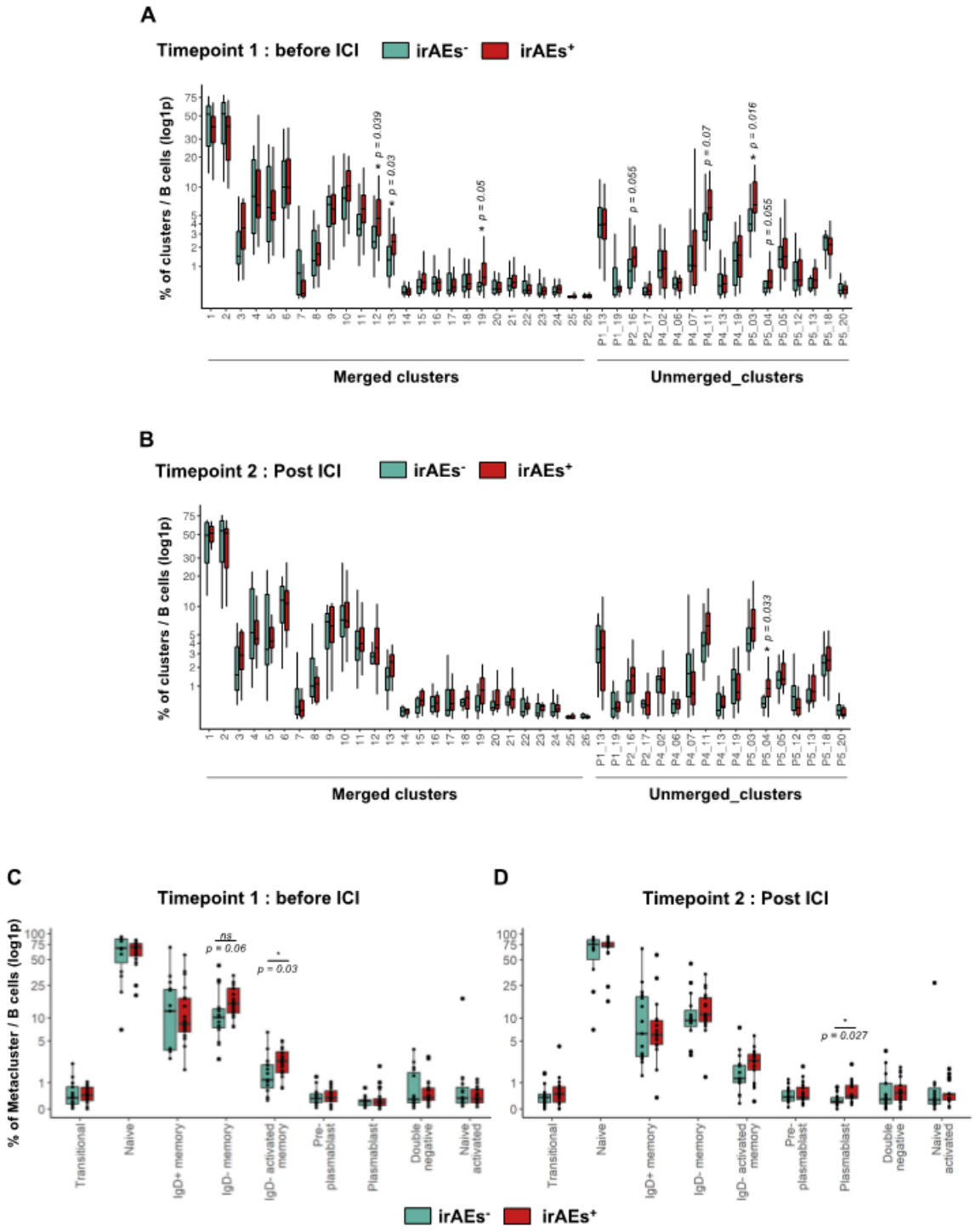


Figure 2

Increased abundance of IgD⁻ memory B cells in patients who developed irAEs prior to ICI initiation. Differential abundance of merged and unmerged B-cell clusters **(A, B)** or B-cell metaclusters **(C, D)** in the PRED_1 cohort. **(A, C)** Before ICI initiation (Timepoint 1; irAEs⁻ n=15; irAEs⁺ n=20) and **(B, D)** 3 weeks after ICI initiation (Timepoint 2; irAEs⁻ n=15; irAEs⁺ n=17). Data are presented as the percentage of each

cluster or metacluster among CD19⁺ B cells. P-values were calculated using the Mann-Whitney-Wilcoxon tests. IrAEs⁻ patients are shown in green and irAEs⁺ patients in red.

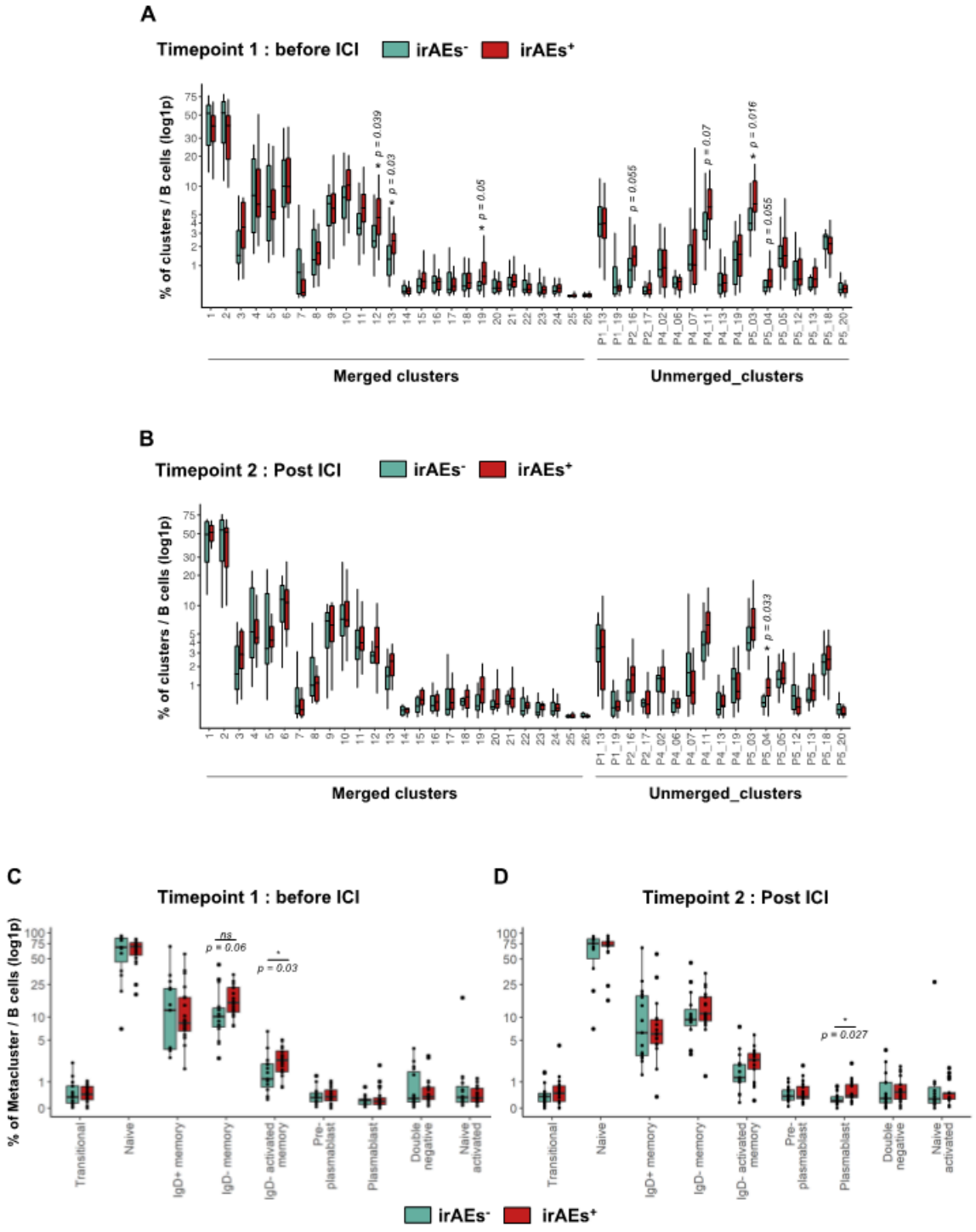


Figure 2

Increased abundance of IgD⁻ memory B cells in patients who developed irAEs prior to ICI initiation. Differential abundance of merged and unmerged B-cell clusters **(A, B)** or B-cell metaclusters **(C, D)** in the

PRED_1 cohort. **(A, C)** Before ICI initiation (Timepoint 1; irAEs⁻ n=15; irAEs⁺ n=20) and **(B, D)** 3 weeks after ICI initiation (Timepoint 2; irAEs⁻ n=15; irAEs⁺ n=17). Data are presented as the percentage of each cluster or metacluster among CD19⁺ B cells. P-values were calculated using the Mann-Whitney-Wilcoxon tests. IrAEs⁻ patients are shown in green and irAEs⁺ patients in red.

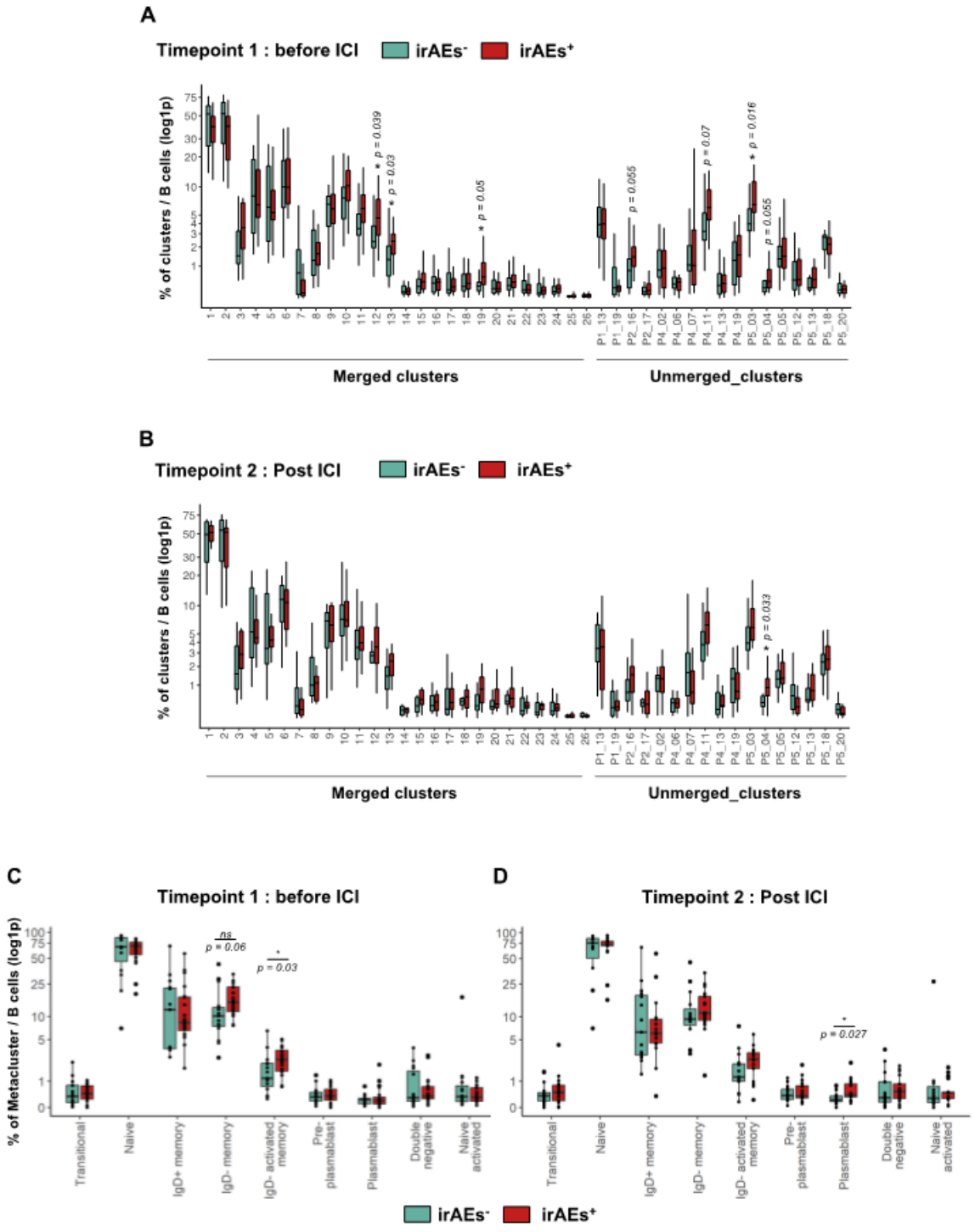


Figure 2

Increased abundance of IgD⁻ memory B cells in patients who developed irAEs prior to ICI initiation. Differential abundance of merged and unmerged B-cell clusters **(A, B)** or B-cell metaclusters **(C, D)** in the PRED_1 cohort. **(A, C)** Before ICI initiation (Timepoint 1; irAEs⁻ n=15; irAEs⁺ n=20) and **(B, D)** 3 weeks after ICI initiation (Timepoint 2; irAEs⁻ n=15; irAEs⁺ n=17). Data are presented as the percentage of each cluster or metacluster among CD19⁺ B cells. P-values were calculated using the Mann-Whitney-Wilcoxon tests. IrAEs⁻ patients are shown in green and irAEs⁺ patients in red.

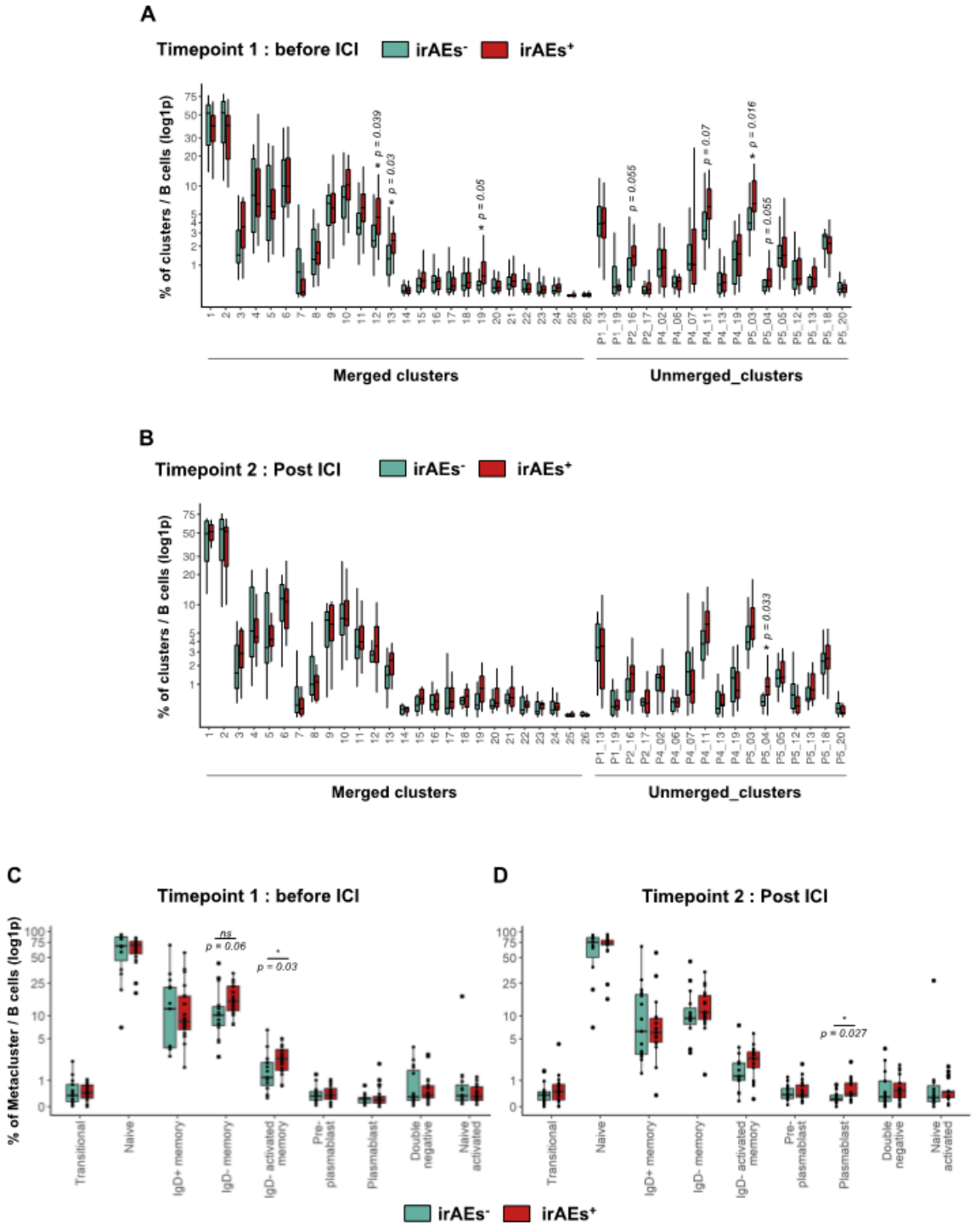


Figure 2

Increased abundance of IgD$^-$ memory B cells in patients who developed irAEs prior to ICI initiation. Differential abundance of merged and unmerged B-cell clusters **(A, B)** or B-cell metaclusters **(C, D)** in the PRED_1 cohort. **(A, C)** Before ICI initiation (Timepoint 1; irAEs$^-$ n=15; irAEs$^+$ n=20) and **(B, D)** 3 weeks after ICI initiation (Timepoint 2; irAEs$^-$ n=15; irAEs$^+$ n=17). Data are presented as the percentage of each cluster or metacluster among CD19$^+$ B cells. P-values were calculated using the Mann-Whitney-Wilcoxon tests. IrAEs$^-$ patients are shown in green and irAEs$^+$ patients in red.

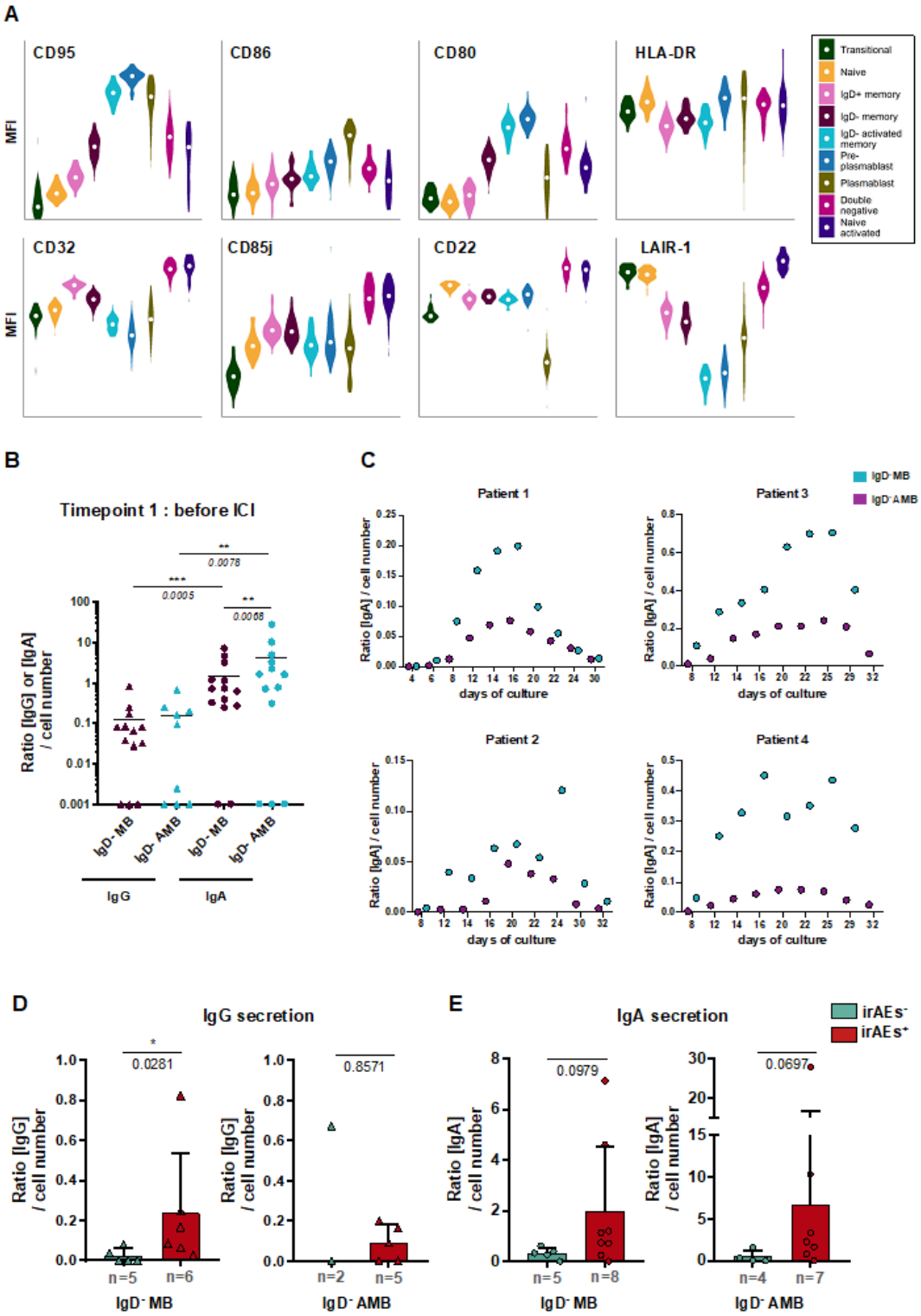


Figure 3

Elevated activation of IgD⁻ MB and IgD⁻ AMB subsets prior to ICI therapy. A, Mean fluorescence intensity (MFI) of activation markers (CD95, CD86, CD80, HLA-DR) and inhibitory markers (CD32, CD85j, CD22, LAIR-1) across B-cell metaclusters in the PRED_1 cohort before ICI initiation (n = 35). Statistical results (two-tailed Wilcoxon signed-rank tests and Bonferroni correction) are summarized in Supplementary Table 8. **B,** IgG and IgA production by sorted and *in vitro*–stimulated IgD⁻ MB and IgD⁻

AMB subsets. Culture supernatants collected from day 4 to day 32 were pooled prior to ELISA quantification. Antibody concentrations (ng/mL) were normalized to the number of sorted B cells. Statistical analysis was performed using two-tailed Wilcoxon signed-rank tests. **C,** Kinetic analysis of IgA production by sorted IgD^- MB and IgD^- AMB cells from four melanoma patients. IgA concentrations were measured in supernatants collected between day 4-8 and day 30–32. **(D, E)** ELISA analysis of IgG **(D)** and IgA **(E)** production by sorted and *in vitro*–stimulated IgD^- MB and IgD^- AMB cells from PRED_1 melanoma patients prior to ICI, stratified according to irAE status ($irAEs^-$, green; $irAEs^+$, red). Antibody concentrations (ng/ml) were normalized to the number of sorted B cells. Statistical analyses were performed using Mann–Whitney–Wilcoxon tests.

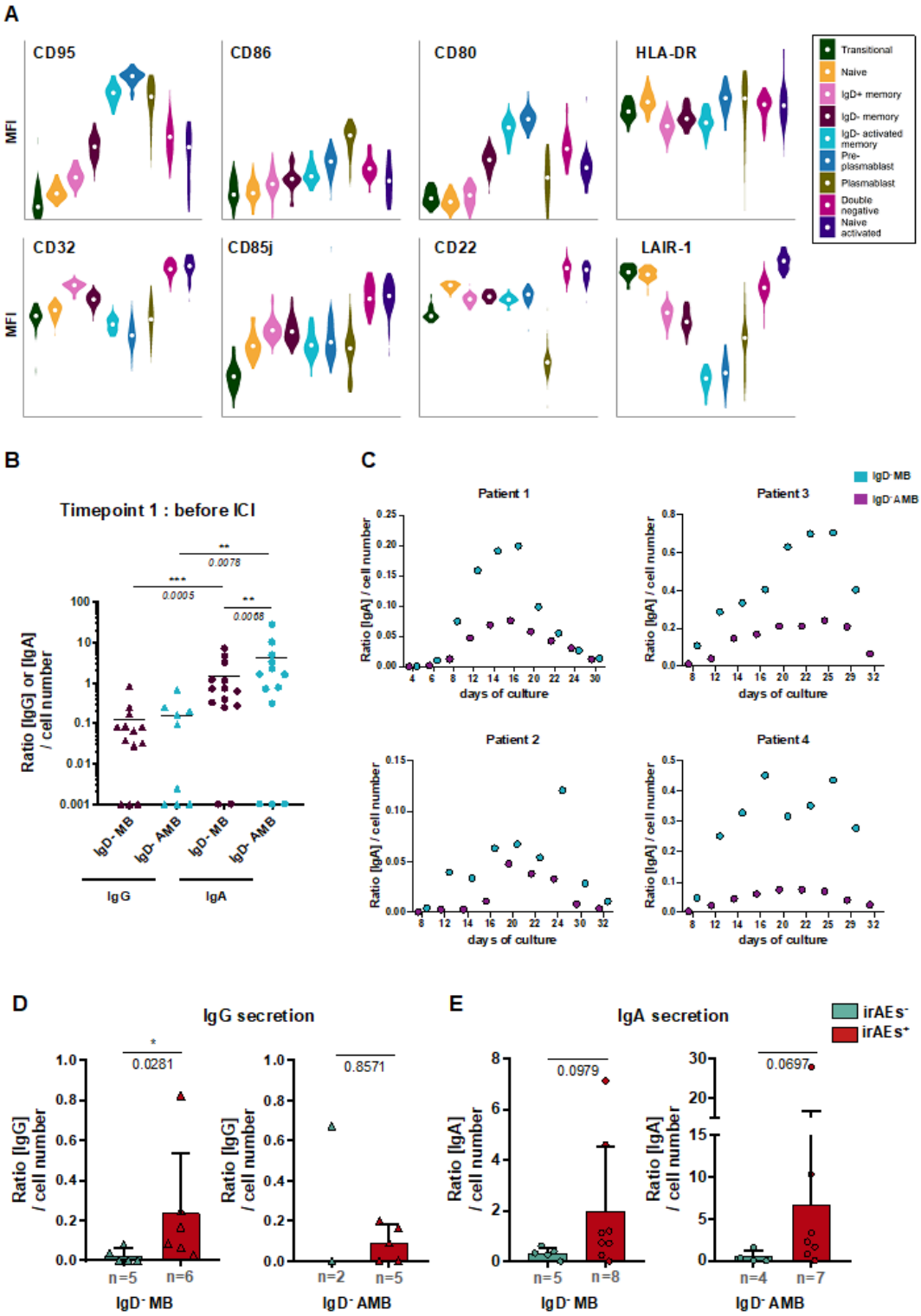


Figure 3

Elevated activation of IgD⁻ MB and IgD⁻ AMB subsets prior to ICI therapy. A, Mean fluorescence intensity (MFI) of activation markers (CD95, CD86, CD80, HLA-DR) and inhibitory markers (CD32, CD85j, CD22, LAIR-1) across B-cell metaclusters in the PRED_1 cohort before ICI initiation (n = 35). Statistical results (two-tailed Wilcoxon signed-rank tests and Bonferroni correction) are summarized in Supplementary Table 8. **B,** IgG and IgA production by sorted and *in vitro*–stimulated IgD⁻ MB and IgD⁻

AMB subsets. Culture supernatants collected from day 4 to day 32 were pooled prior to ELISA quantification. Antibody concentrations (ng/mL) were normalized to the number of sorted B cells. Statistical analysis was performed using two-tailed Wilcoxon signed-rank tests. **C,** Kinetic analysis of IgA production by sorted IgD^- MB and IgD^- AMB cells from four melanoma patients. IgA concentrations were measured in supernatants collected between day 4-8 and day 30–32. **(D, E)** ELISA analysis of IgG **(D)** and IgA **(E)** production by sorted and *in vitro*–stimulated IgD^- MB and IgD^- AMB cells from PRED_1 melanoma patients prior to ICI, stratified according to irAE status ($irAEs^-$, green; $irAEs^+$, red). Antibody concentrations (ng/ml) were normalized to the number of sorted B cells. Statistical analyses were performed using Mann–Whitney–Wilcoxon tests.

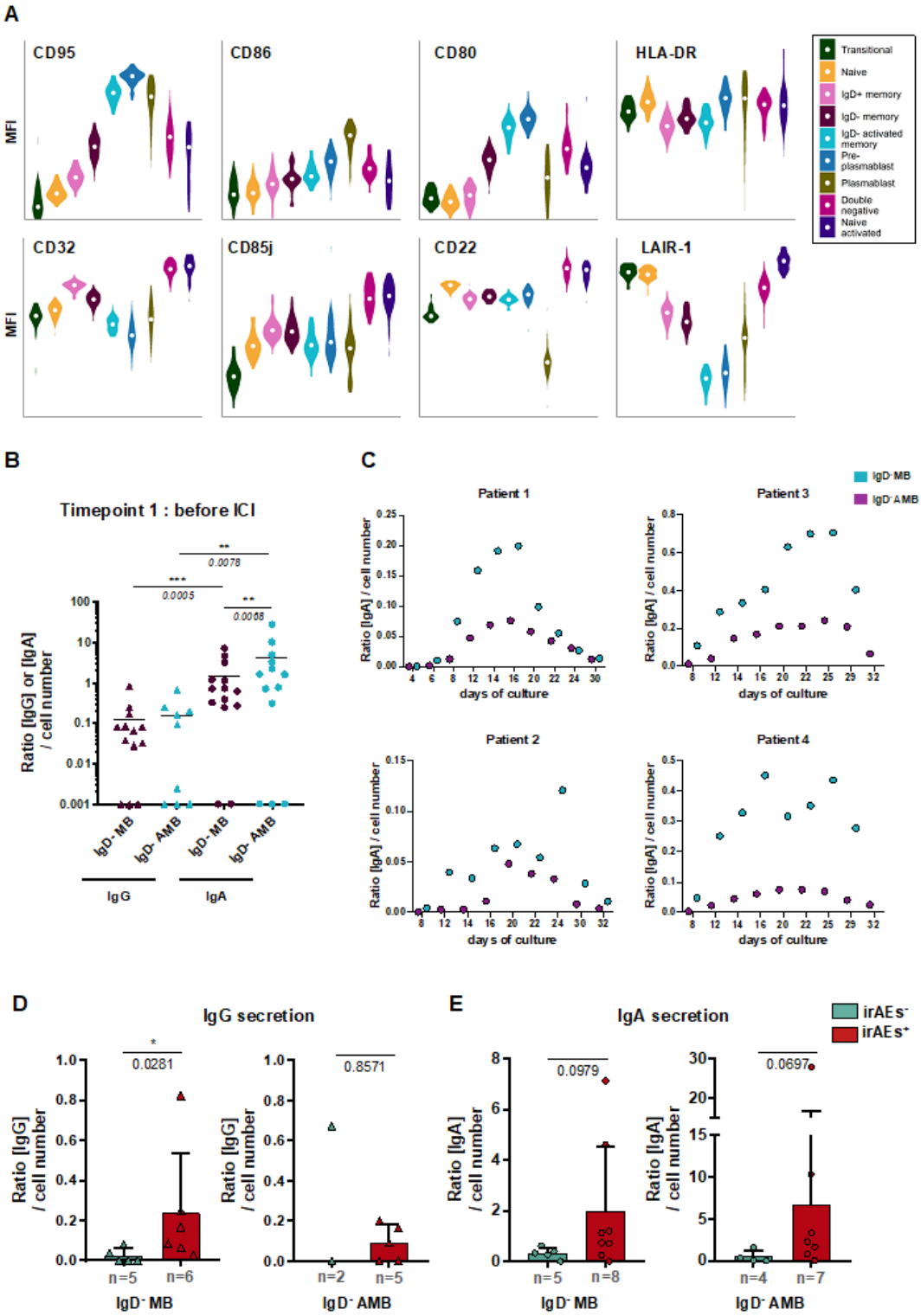


Figure 3

Elevated activation of IgD⁻ MB and IgD⁻ AMB subsets prior to ICI therapy. A, Mean fluorescence intensity (MFI) of activation markers (CD95, CD86, CD80, HLA-DR) and inhibitory markers (CD32, CD85j, CD22, LAIR-1) across B-cell metaclusters in the PRED_1 cohort before ICI initiation (n = 35). Statistical results (two-tailed Wilcoxon signed-rank tests and Bonferroni correction) are summarized in Supplementary Table 8. **B,** IgG and IgA production by sorted and *in vitro*–stimulated IgD⁻ MB and IgD⁻

AMB subsets. Culture supernatants collected from day 4 to day 32 were pooled prior to ELISA quantification. Antibody concentrations (ng/mL) were normalized to the number of sorted B cells. Statistical analysis was performed using two-tailed Wilcoxon signed-rank tests. **C,** Kinetic analysis of IgA production by sorted IgD^- MB and IgD^- AMB cells from four melanoma patients. IgA concentrations were measured in supernatants collected between day 4-8 and day 30–32. **(D, E)** ELISA analysis of IgG **(D)** and IgA **(E)** production by sorted and *in vitro*–stimulated IgD^- MB and IgD^- AMB cells from PRED_1 melanoma patients prior to ICI, stratified according to irAE status ($irAEs^-$, green; $irAEs^+$, red). Antibody concentrations (ng/ml) were normalized to the number of sorted B cells. Statistical analyses were performed using Mann–Whitney–Wilcoxon tests.

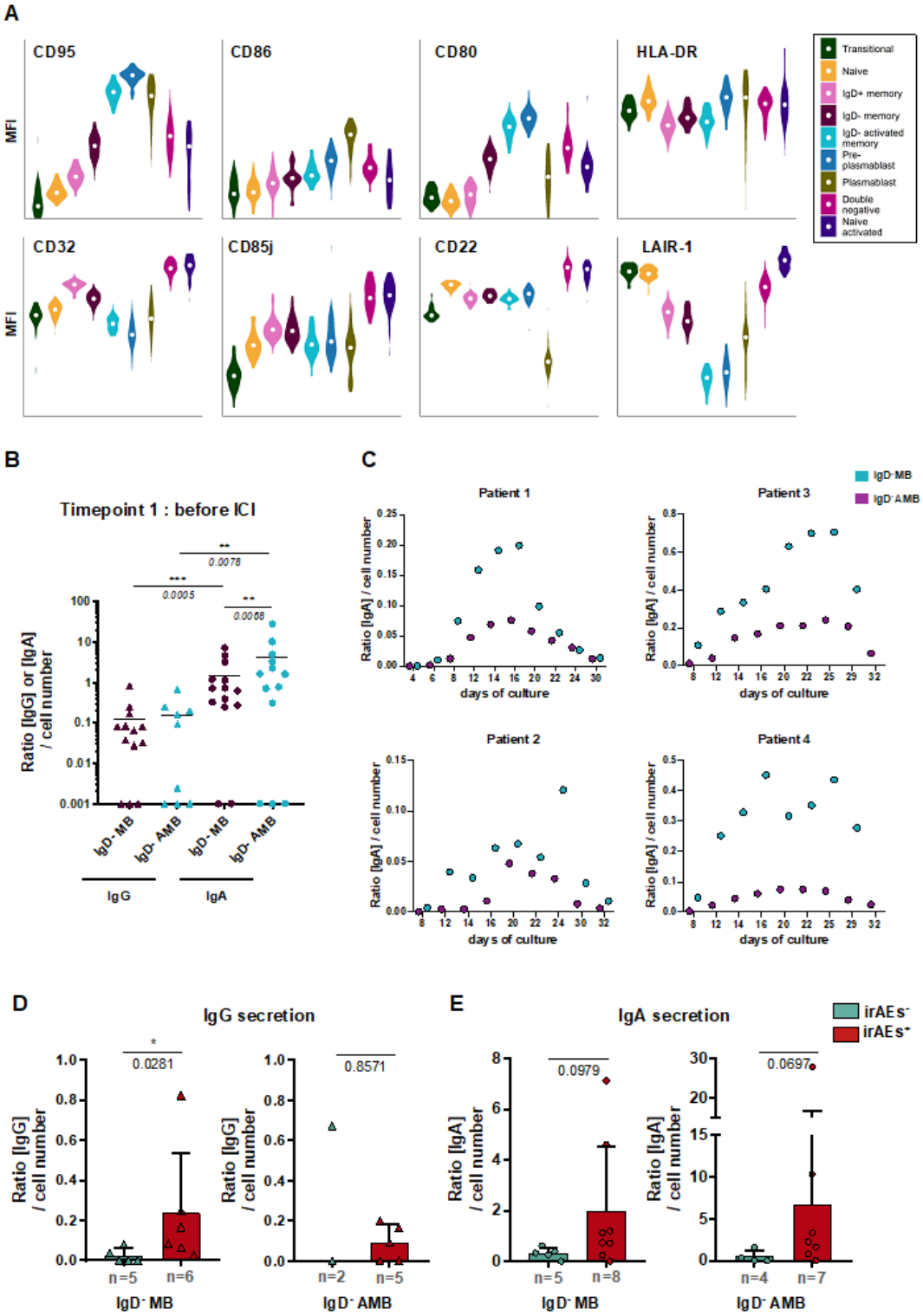


Figure 3

Elevated activation of IgD⁻ MB and IgD⁻ AMB subsets prior to ICI therapy. A, Mean fluorescence intensity (MFI) of activation markers (CD95, CD86, CD80, HLA-DR) and inhibitory markers (CD32, CD85j, CD22, LAIR-1) across B-cell metaclusters in the PRED_1 cohort before ICI initiation (n = 35). Statistical results (two-tailed Wilcoxon signed-rank tests and Bonferroni correction) are summarized in Supplementary Table 8. **B,** IgG and IgA production by sorted and *in vitro*–stimulated IgD⁻ MB and IgD⁻

AMB subsets. Culture supernatants collected from day 4 to day 32 were pooled prior to ELISA quantification. Antibody concentrations (ng/mL) were normalized to the number of sorted B cells. Statistical analysis was performed using two-tailed Wilcoxon signed-rank tests. **C,** Kinetic analysis of IgA production by sorted IgD$^-$ MB and IgD$^-$ AMB cells from four melanoma patients. IgA concentrations were measured in supernatants collected between day 4-8 and day 30–32. **(D, E)** ELISA analysis of IgG **(D)** and IgA **(E)** production by sorted and *in vitro*–stimulated IgD$^-$ MB and IgD$^-$ AMB cells from PRED_1 melanoma patients prior to ICI, stratified according to irAE status (irAEs$^-$, green; irAEs$^+$, red). Antibody concentrations (ng/ml) were normalized to the number of sorted B cells. Statistical analyses were performed using Mann–Whitney–Wilcoxon tests.

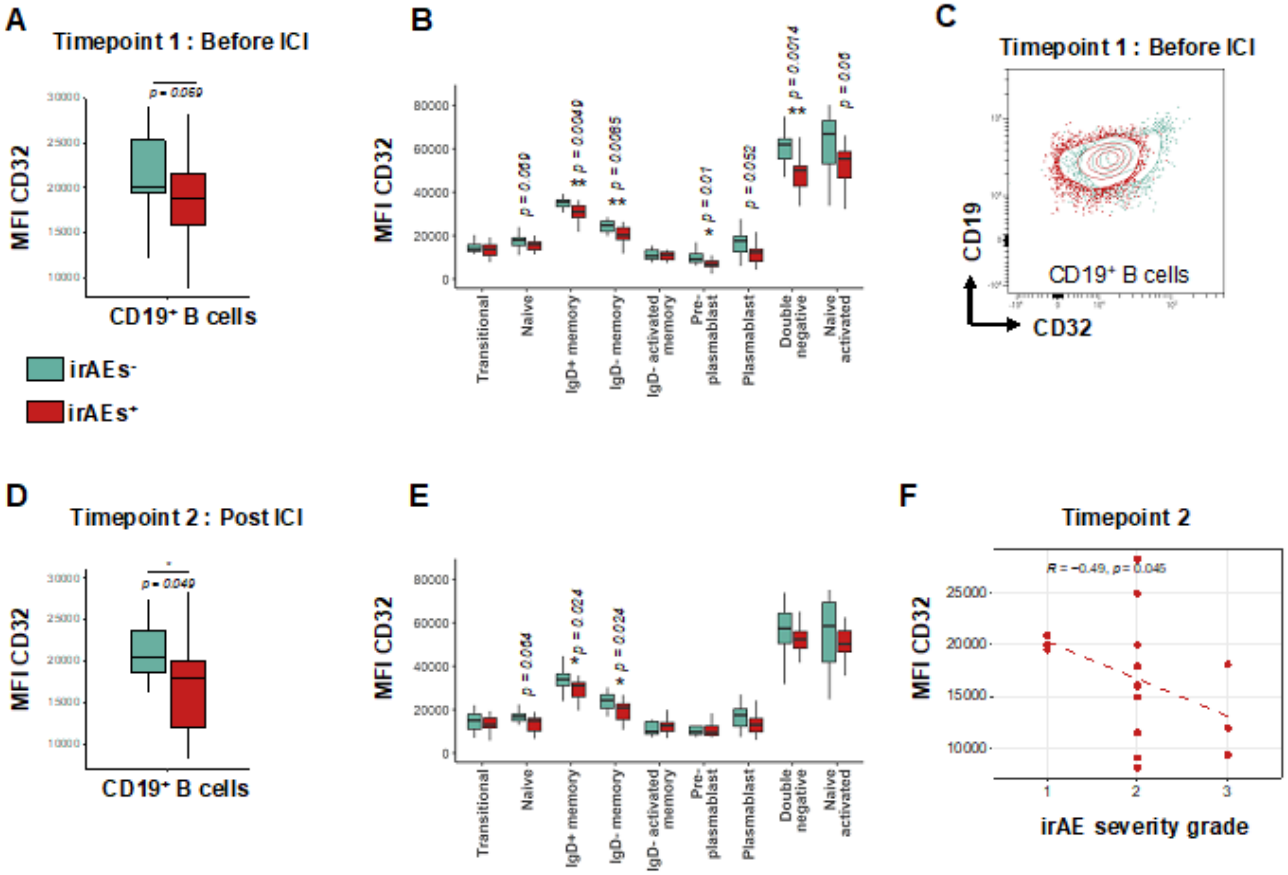


Figure 4

Reduced expression of FcgRIIB inhibitory receptor on peripheral B-cell subsets in irAEs$^+$ patients. FcgRIIB (CD32) expression was measured before ICI (Timepoint 1; irAEs$^-$ n=15; irAEs$^+$ n=20) and 3-weeks post-ICI initiation (Timepoint 2; irAEs$^-$ n=15; irAEs$^+$ n=17). (**A and D)** MFI of FcγRIIB expression on total CD19$^+$ B cells before **(A)** and post-treatment **(D)**. **(B and E)** MFI of FcγRIIB expression on B-cell metaclusters before **(B)** and post-treatment **(E)**. PRED_1 patients are grouped by irAE status (irAEs$^-$, green; irAEs$^+$, red). Statistical comparisons were performed using Mann-Whitney-Wilcoxon tests. P-

values are shown above box plots. **C,** Representative dot plot of FcγRIIB expression on total CD19⁺ B cells pre-treatment in one irAEs⁻ patient (green) versus one irAEs⁺ patient (red). **F,** Spearman correlation between CD32 expression on CD19⁺ B cells at Timepoint 2 and irAE severity (n=4 grade 1, n=10 grade 2 and n=3 grade 3).

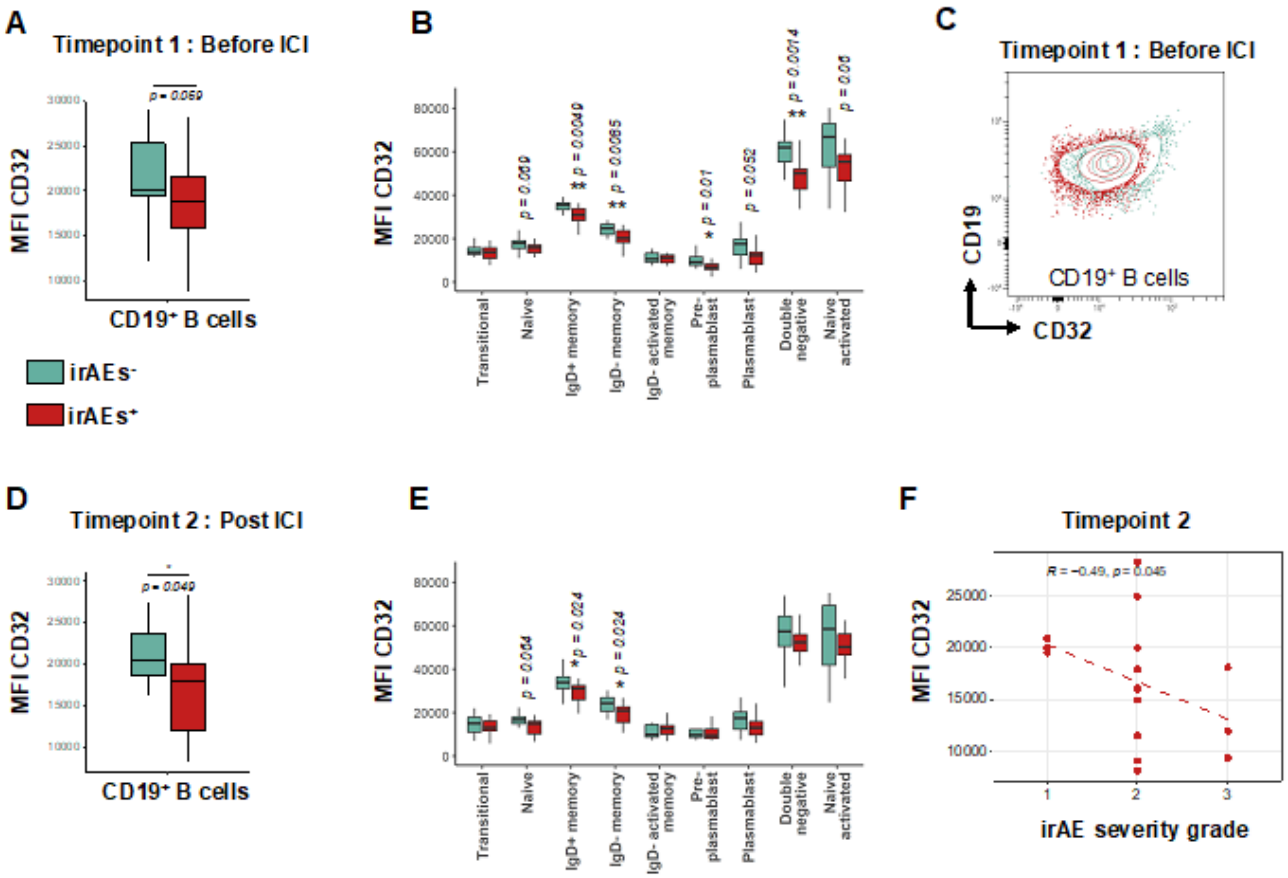


Figure 4

Reduced expression of FcgRIIB inhibitory receptor on peripheral B-cell subsets in irAEs⁺ patients. FcgRIIB (CD32) expression was measured before ICI (Timepoint 1; irAEs⁻ n=15; irAEs⁺ n=20) and 3-weeks post-ICI initiation (Timepoint 2; irAEs⁻ n=15; irAEs⁺ n=17). (**A and D)** MFI of FcγRIIB expression on total CD19⁺ B cells before **(A)** and post-treatment **(D)**. **(B and E)** MFI of FcγRIIB expression on B-cell metaclusters before **(B)** and post-treatment **(E)**. PRED_1 patients are grouped by irAE status (irAEs⁻, green; irAEs⁺, red). Statistical comparisons were performed using Mann-Whitney-Wilcoxon tests. P-values are shown above box plots. **C,** Representative dot plot of FcγRIIB expression on total CD19⁺ B cells pre-treatment in one irAEs⁻ patient (green) versus one irAEs⁺ patient (red). **F,** Spearman correlation

between CD32 expression on CD19^{+} B cells at Timepoint 2 and irAE severity (n=4 grade 1, n=10 grade 2 and n=3 grade 3).

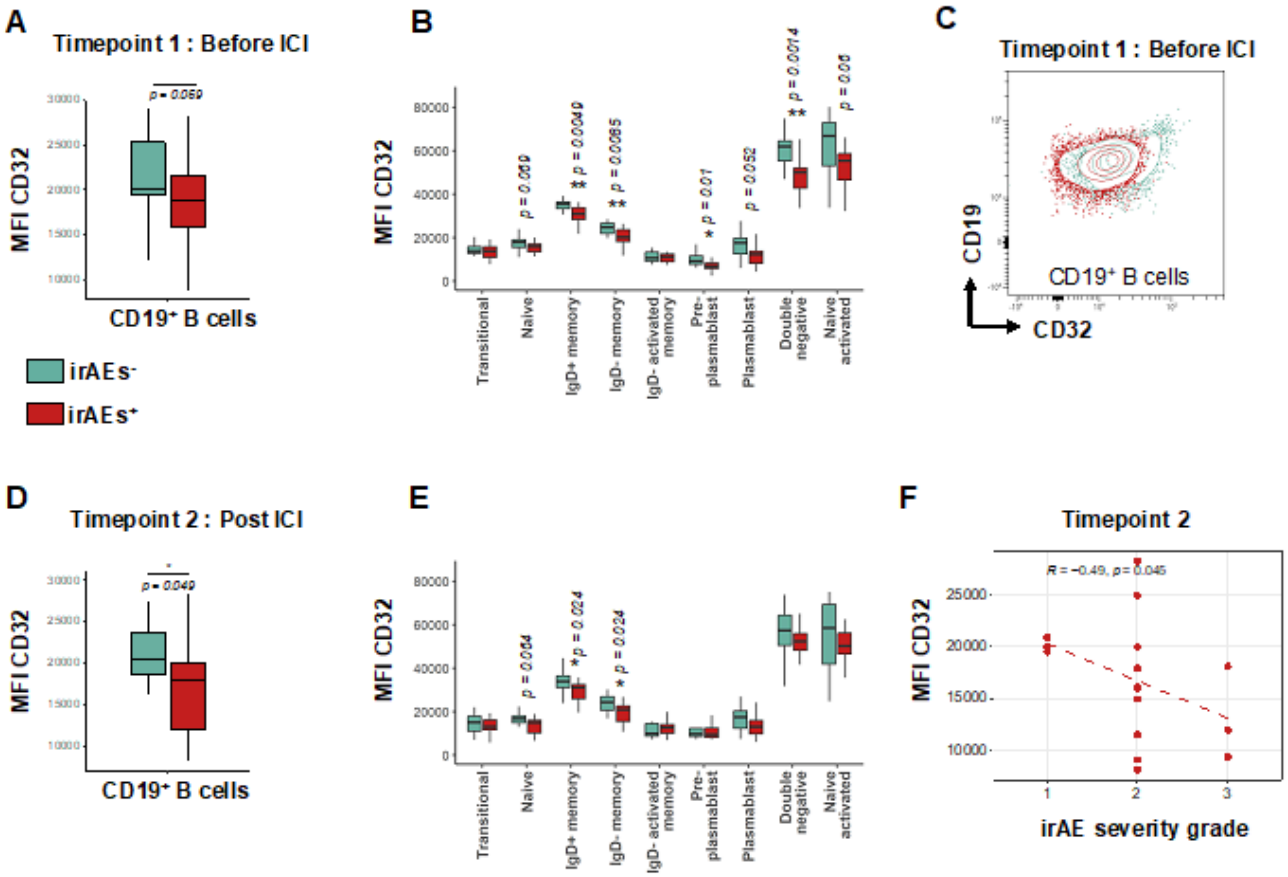


Figure 4

Reduced expression of FcgRIIB inhibitory receptor on peripheral B-cell subsets in irAEs^{+} patients. FcgRIIB (CD32) expression was measured before ICI (Timepoint 1; irAEs^{-} n=15; irAEs^{+} n=20) and 3-weeks post-ICI initiation (Timepoint 2; irAEs^{-} n=15; irAEs^{+} n=17). (**A and D)** MFI of FcγRIIB expression on total CD19^{+} B cells before **(A)** and post-treatment **(D)**. **(B and E)** MFI of FcγRIIB expression on B-cell metaclusters before **(B)** and post-treatment **(E)**. PRED_1 patients are grouped by irAE status (irAEs^{-}, green; irAEs^{+}, red). Statistical comparisons were performed using Mann-Whitney-Wilcoxon tests. P-values are shown above box plots. **C,** Representative dot plot of FcγRIIB expression on total CD19^{+} B cells pre-treatment in one irAEs^{-} patient (green) versus one irAEs^{+} patient (red). **F,** Spearman correlation between CD32 expression on CD19^{+} B cells at Timepoint 2 and irAE severity (n=4 grade 1, n=10 grade 2 and n=3 grade 3).

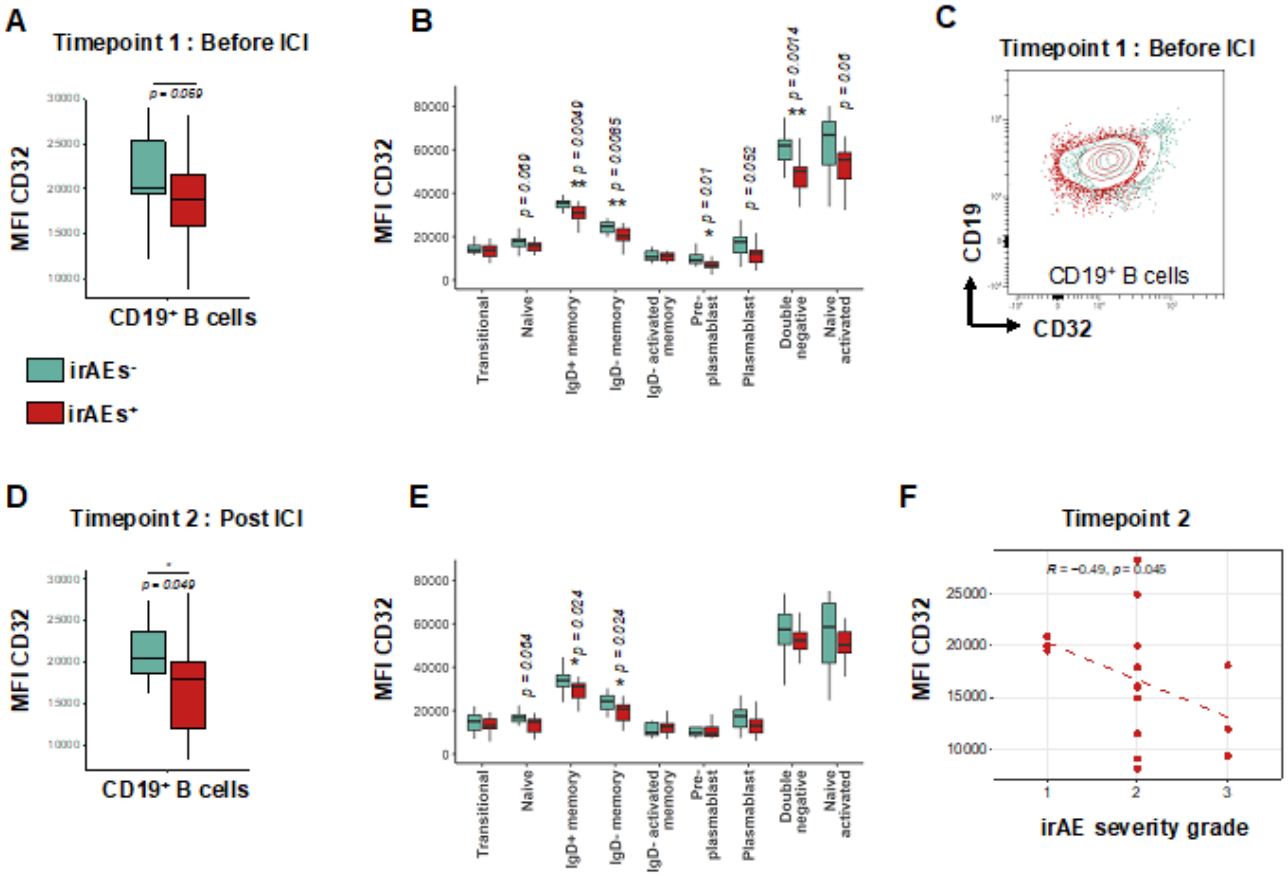


Figure 4

Reduced expression of FcgRIIB inhibitory receptor on peripheral B-cell subsets in irAEs$^+$ patients. FcgRIIB (CD32) expression was measured before ICI (Timepoint 1; irAEs$^-$ n=15; irAEs$^+$ n=20) and 3-weeks post-ICI initiation (Timepoint 2; irAEs$^-$ n=15; irAEs$^+$ n=17). (**A and D)** MFI of FcγRIIB expression on total CD19$^+$ B cells before **(A)** and post-treatment **(D)**. **(B and E)** MFI of FcγRIIB expression on B-cell metaclusters before **(B)** and post-treatment **(E)**. PRED_1 patients are grouped by irAE status (irAEs$^-$, green; irAEs$^+$, red). Statistical comparisons were performed using Mann-Whitney-Wilcoxon tests. P-values are shown above box plots. **C,** Representative dot plot of FcγRIIB expression on total CD19$^+$ B cells pre-treatment in one irAEs$^-$ patient (green) versus one irAEs$^+$ patient (red). **F,** Spearman correlation between CD32 expression on CD19$^+$ B cells at Timepoint 2 and irAE severity (n=4 grade 1, n=10 grade 2 and n=3 grade 3).

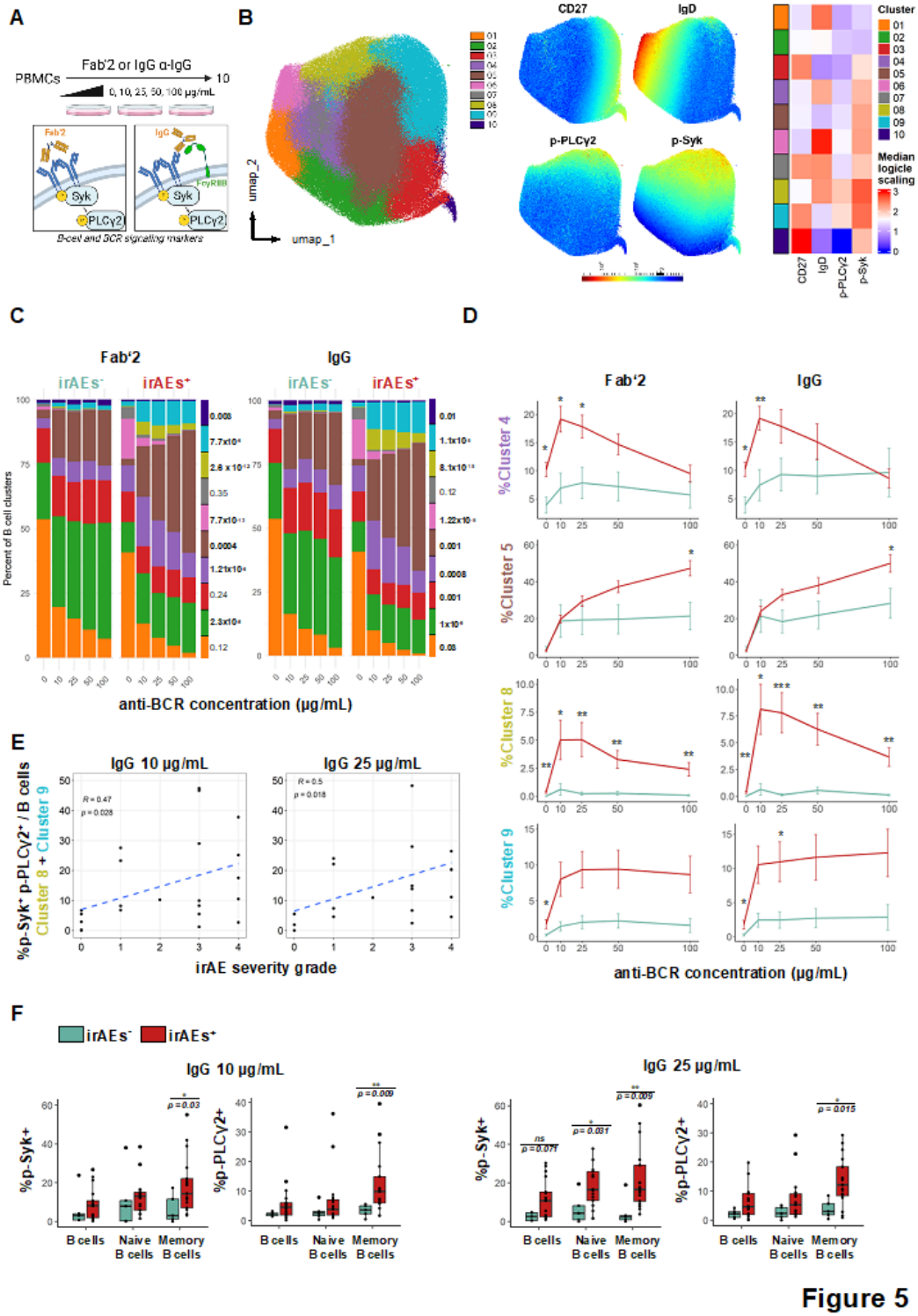


Figure 5

Figure 5

Peripheral memory B cells from irAEs$^+$ patients display increased activation sensitivity prior to ICI initiation. A, Experimental design of kinase phosphorylation assays performed in PRED_2 patients before ICI initiation (irAEs$^-$ n=5; irAEs$^+$ n=17). Left: F(ab')$_2$ anti-BCR fragments selectively engage the BCR and induce phosphorylation of Syk (p-Syk) and PLCγ2 (p-PLCγ2). Right: Full IgG anti-BCR antibody co-

engage BCR and FcγRIIB. *Created with Biorender.com.* PBMCs were stimulated for 10 minutes with Fab'_2 or IgG anti-IgG (0, 10, 25, 50 or 100 µg/mL) and analyzed by flow cytometry. $CD19^+$ B cells were gated as single, live $CD45^+CD3^-CD14^-CD19^+$ cells. **B,** Unsupervised analysis of $CD19^+$ B cells identified ten B-cell clusters. Left: UMAP representation of FlowSOM clusters. Right: UMAP projections and heatmap showing scaled marker expression (red, highest; blue, lowest). **C,** Mean frequency of the ten B-cell clusters across stimulation conditions, grouped by irAE status and color-coded as in **(B)**. Global differences in cluster frequencies between groups were assessed using a rank-based linear mixed-effects model. Corresponding p-values for each cluster are indicated alongside the graphs. **D**, Abundance (mean ± SEM) of clusters 4, 5, 8 and 9 ($p\text{-}Syk^+$ and/or $p\text{-}PLC\gamma2^+$) among $CD19^+$ B cells in $irAEs^-$ (green) and $irAEs^+$ (red) patients at each stimulation dose. Statistical comparisons for the ten clusters were performed using Mann-Whitney-Wilcoxon tests and are summarized in Supplementary Table 12a. **E**, Spearman correlations between the abundance of $p\text{-}Syk^+$ $p\text{-}PLC\gamma2^+$ clusters (clusters 8 and 9) and irAE severity (n=5 no toxicity, n=4 grade 1, n=1 grade 2, n=7 grade 3 and n=5 grade 4) following stimulation with IgG anti-BCR (10 or 25 µg/mL). **F**, Percentages of $p\text{-}Syk^+$ and $p\text{-}PLC\gamma2^+$ cells among $CD19^+$ B cells, naïve $CD19^+CD27^-IgD^+$ B cells, and memory $CD19^+CD27^+IgD^-$ B cells after IgG anti-BCR stimulation (10 or 25 µg/mL) in $irAEs^-$ (green) and $irAEs^+$ (red) patients. Statistical analyses were performed using Mann-Whitney-Wilcoxon tests and are summarized in Supplementary Table 12b.

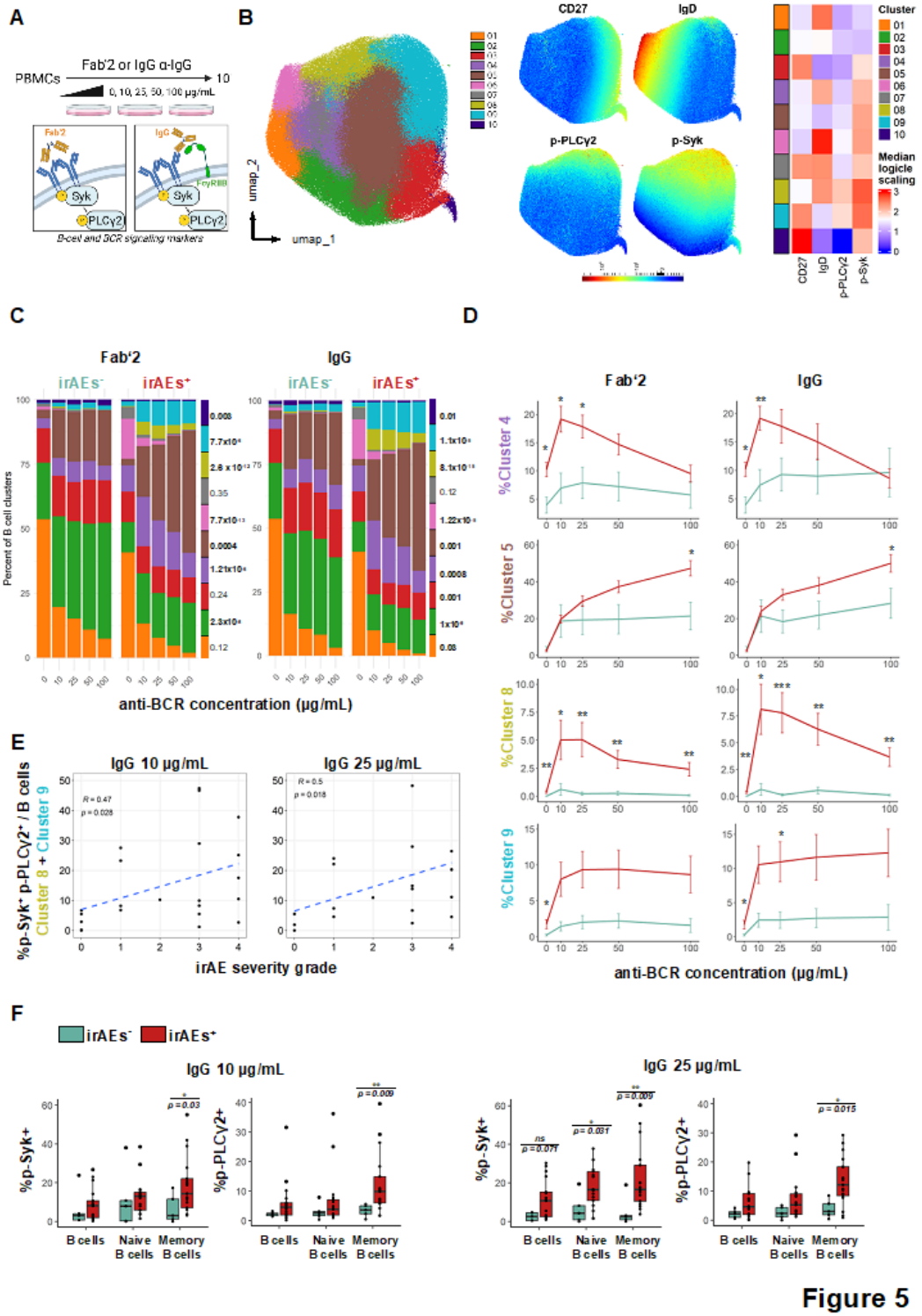


Figure 5

Figure 5

Peripheral memory B cells from irAEs$^+$ patients display increased activation sensitivity prior to ICI initiation. A, Experimental design of kinase phosphorylation assays performed in PRED_2 patients before ICI initiation (irAEs$^-$ n=5; irAEs$^+$ n=17). Left: F(ab')$_2$ anti-BCR fragments selectively engage the BCR and induce phosphorylation of Syk (p-Syk) and PLCγ2 (p-PLCγ2). Right: Full IgG anti-BCR antibody co-

engage BCR and FcγRIIB. *Created with Biorender.com.* PBMCs were stimulated for 10 minutes with Fab'_2 or IgG anti-IgG (0, 10, 25, 50 or 100 µg/mL) and analyzed by flow cytometry. $CD19^+$ B cells were gated as single, live $CD45^+CD3^-CD14^-CD19^+$ cells. **B,** Unsupervised analysis of $CD19^+$ B cells identified ten B-cell clusters. Left: UMAP representation of FlowSOM clusters. Right: UMAP projections and heatmap showing scaled marker expression (red, highest; blue, lowest). **C,** Mean frequency of the ten B-cell clusters across stimulation conditions, grouped by irAE status and color-coded as in **(B)**. Global differences in cluster frequencies between groups were assessed using a rank-based linear mixed-effects model. Corresponding p-values for each cluster are indicated alongside the graphs. **D**, Abundance (mean ± SEM) of clusters 4, 5, 8 and 9 ($p\text{-}Syk^+$ and/or $p\text{-}PLC\gamma2^+$) among $CD19^+$ B cells in $irAEs^-$ (green) and $irAEs^+$ (red) patients at each stimulation dose. Statistical comparisons for the ten clusters were performed using Mann-Whitney-Wilcoxon tests and are summarized in Supplementary Table 12a. **E**, Spearman correlations between the abundance of $p\text{-}Syk^+$ $p\text{-}PLC\gamma2^+$ clusters (clusters 8 and 9) and irAE severity (n=5 no toxicity, n=4 grade 1, n=1 grade 2, n=7 grade 3 and n=5 grade 4) following stimulation with IgG anti-BCR (10 or 25 µg/mL). **F**, Percentages of $p\text{-}Syk^+$ and $p\text{-}PLC\gamma2^+$ cells among $CD19^+$ B cells, naïve $CD19^+CD27^-IgD^+$ B cells, and memory $CD19^+CD27^+IgD^-$ B cells after IgG anti-BCR stimulation (10 or 25 µg/mL) in $irAEs^-$ (green) and $irAEs^+$ (red) patients. Statistical analyses were performed using Mann-Whitney-Wilcoxon tests and are summarized in Supplementary Table 12b.

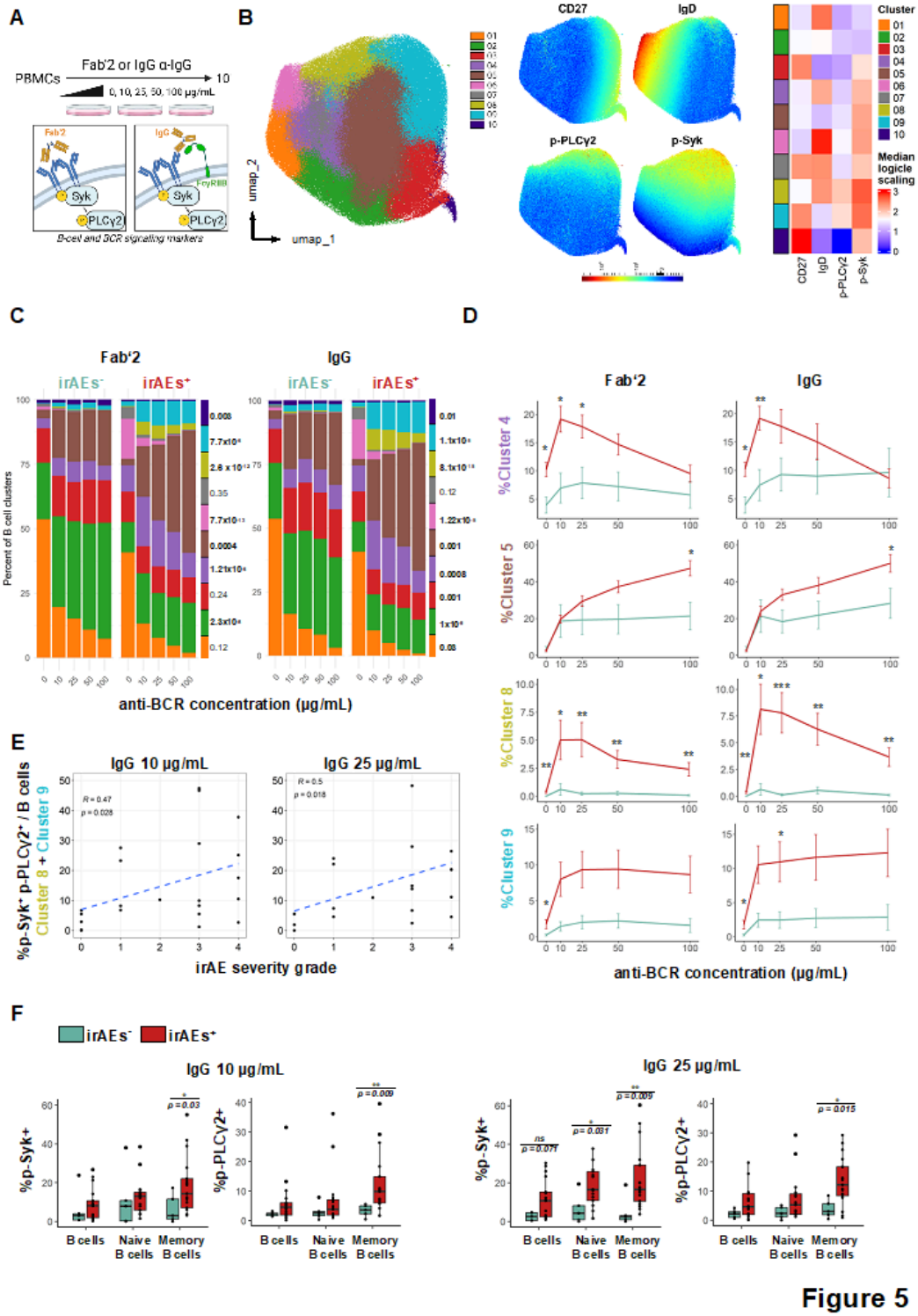


Figure 5

Figure 5

Peripheral memory B cells from irAEs$^+$ patients display increased activation sensitivity prior to ICI initiation. A, Experimental design of kinase phosphorylation assays performed in PRED_2 patients before ICI initiation (irAEs$^-$ n=5; irAEs$^+$ n=17). Left: F(ab')$_2$ anti-BCR fragments selectively engage the BCR and induce phosphorylation of Syk (p-Syk) and PLCγ2 (p-PLCγ2). Right: Full IgG anti-BCR antibody co-

engage BCR and FcγRIIB. *Created with Biorender.com.* PBMCs were stimulated for 10 minutes with Fab'_2 or IgG anti-IgG (0, 10, 25, 50 or 100 µg/mL) and analyzed by flow cytometry. $CD19^+$ B cells were gated as single, live $CD45^+CD3^-CD14^-CD19^+$ cells. **B,** Unsupervised analysis of $CD19^+$ B cells identified ten B-cell clusters. Left: UMAP representation of FlowSOM clusters. Right: UMAP projections and heatmap showing scaled marker expression (red, highest; blue, lowest). **C,** Mean frequency of the ten B-cell clusters across stimulation conditions, grouped by irAE status and color-coded as in **(B)**. Global differences in cluster frequencies between groups were assessed using a rank-based linear mixed-effects model. Corresponding p-values for each cluster are indicated alongside the graphs. **D**, Abundance (mean ± SEM) of clusters 4, 5, 8 and 9 ($p\text{-}Syk^+$ and/or $p\text{-}PLC\gamma2^+$) among $CD19^+$ B cells in $irAEs^-$ (green) and $irAEs^+$ (red) patients at each stimulation dose. Statistical comparisons for the ten clusters were performed using Mann-Whitney-Wilcoxon tests and are summarized in Supplementary Table 12a. **E**, Spearman correlations between the abundance of $p\text{-}Syk^+$ $p\text{-}PLC\gamma2^+$ clusters (clusters 8 and 9) and irAE severity (n=5 no toxicity, n=4 grade 1, n=1 grade 2, n=7 grade 3 and n=5 grade 4) following stimulation with IgG anti-BCR (10 or 25 µg/mL). **F**, Percentages of $p\text{-}Syk^+$ and $p\text{-}PLC\gamma2^+$ cells among $CD19^+$ B cells, naïve $CD19^+CD27^-IgD^+$ B cells, and memory $CD19^+CD27^+IgD^-$ B cells after IgG anti-BCR stimulation (10 or 25 µg/mL) in $irAEs^-$ (green) and $irAEs^+$ (red) patients. Statistical analyses were performed using Mann-Whitney-Wilcoxon tests and are summarized in Supplementary Table 12b.

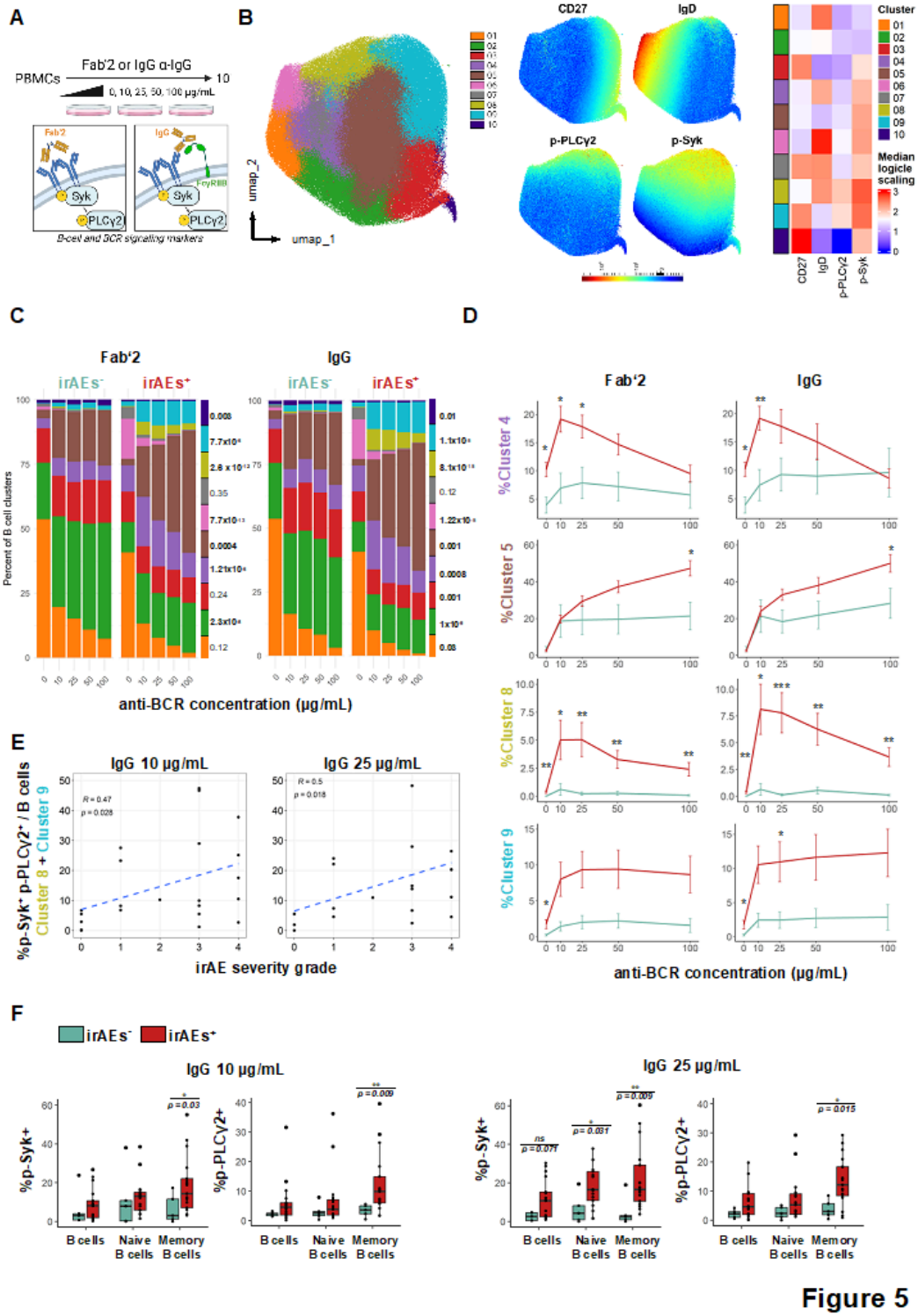


Figure 5

Figure 5

Peripheral memory B cells from irAEs$^+$ patients display increased activation sensitivity prior to ICI initiation. A, Experimental design of kinase phosphorylation assays performed in PRED_2 patients before ICI initiation (irAEs$^-$ n=5; irAEs$^+$ n=17). Left: F(ab')$_2$ anti-BCR fragments selectively engage the BCR and induce phosphorylation of Syk (p-Syk) and PLCγ2 (p-PLCγ2). Right: Full IgG anti-BCR antibody co-

engage BCR and FcγRIIB. *Created with Biorender.com.* PBMCs were stimulated for 10 minutes with Fab'_2 or IgG anti-IgG (0, 10, 25, 50 or 100 µg/mL) and analyzed by flow cytometry. $CD19^+$ B cells were gated as single, live $CD45^+CD3^-CD14^-CD19^+$ cells. **B,** Unsupervised analysis of $CD19^+$ B cells identified ten B-cell clusters. Left: UMAP representation of FlowSOM clusters. Right: UMAP projections and heatmap showing scaled marker expression (red, highest; blue, lowest). **C,** Mean frequency of the ten B-cell clusters across stimulation conditions, grouped by irAE status and color-coded as in **(B)**. Global differences in cluster frequencies between groups were assessed using a rank-based linear mixed-effects model. Corresponding p-values for each cluster are indicated alongside the graphs. **D**, Abundance (mean ± SEM) of clusters 4, 5, 8 and 9 ($p\text{-}Syk^+$ and/or $p\text{-}PLC\gamma2^+$) among $CD19^+$ B cells in $irAEs^-$ (green) and $irAEs^+$ (red) patients at each stimulation dose. Statistical comparisons for the ten clusters were performed using Mann-Whitney-Wilcoxon tests and are summarized in Supplementary Table 12a. **E**, Spearman correlations between the abundance of $p\text{-}Syk^+$ $p\text{-}PLC\gamma2^+$ clusters (clusters 8 and 9) and irAE severity (n=5 no toxicity, n=4 grade 1, n=1 grade 2, n=7 grade 3 and n=5 grade 4) following stimulation with IgG anti-BCR (10 or 25 µg/mL). **F**, Percentages of $p\text{-}Syk^+$ and $p\text{-}PLC\gamma2^+$ cells among $CD19^+$ B cells, naïve $CD19^+CD27^-IgD^+$ B cells, and memory $CD19^+CD27^+IgD^-$ B cells after IgG anti-BCR stimulation (10 or 25 µg/mL) in $irAEs^-$ (green) and $irAEs^+$ (red) patients. Statistical analyses were performed using Mann-Whitney-Wilcoxon tests and are summarized in Supplementary Table 12b.

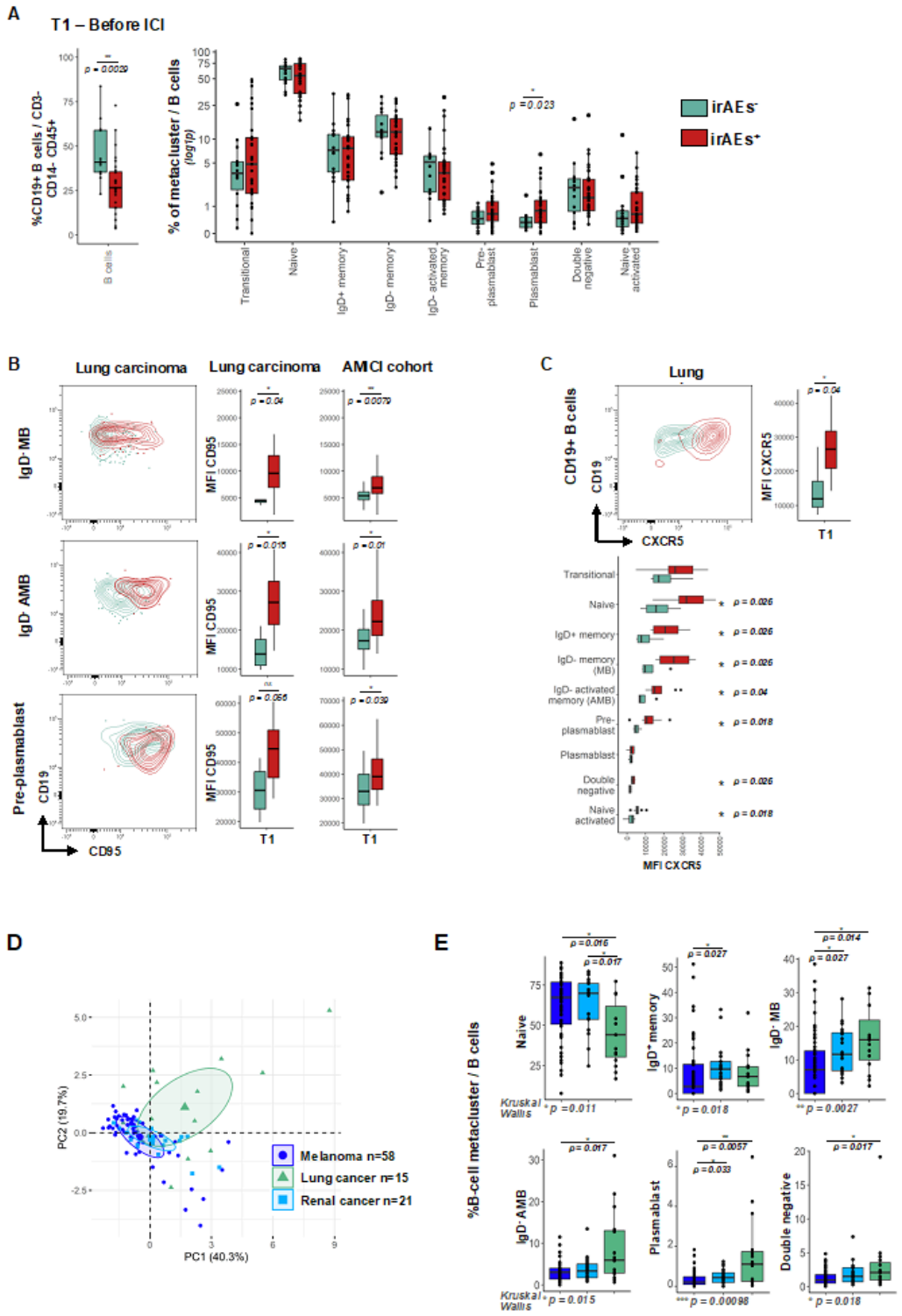


Figure 6

Pan-cancer analysis reveals distinct B-cell activation profiles associated with irAEs. A, Abundance of $CD19^+$ B cells and B-cell metaclusters before ICI (T1) in $irAEs^-$ (n=14) and $irAEs^+$ (n=31) patients from the AMICI pan-cancer cohort. PBMCs were stained with antibody panels 1-5 and analyzed by spectral flow cytometry. Cells were gated as single, live $CD45^+CD3^-CD14^-CD19^+$ B cells. Metaclusters were assigned based on the PRED_1 cohort analysis. **B**, left: Representative dot plots of CD95 and CD19 expression on

IgD$^-$ MB, IgD$^-$ AMB and pre-plasmablasts from irAEs$^-$ (green) and irAEs$^+$ (red) lung carcinoma patients. Right: MFI of CD95 on these subsets is shown for lung carcinoma patients (n=4 irAEs$^-$; n=11 irAEs$^+$) and for all AMICI patients. **C**, Representative CXCR5/CD19 dot plots and CXCR5 MFI on CD19$^+$ B cells and B-cell metaclusters from irAEs$^-$ (green) and irAEs$^+$ (red) lung carcinoma patients. Statistical analyses (summarized in Supplementary Table 13) were performed using Mann-Whitney-Wilcoxon tests; p-values are shown. **D,** Principal component analysis (PCA) of B-cell metacluster abundance colored by cancer type (n=58 melanoma, dark blue; n=15 lung cancer, green; n=21 renal cancer, light blue). **E**, Box plots of B-cell metacluster abundance across melanoma, renal cancer and lung cancer patients. P-values derive from Kruskal-Wallis tests with post hoc Bonferroni-corrected Wilcoxon rank-sum tests. Panels D-E integrate B-cell metacluster data from three cohorts (PRED_1, PRED_2 and AMICI).

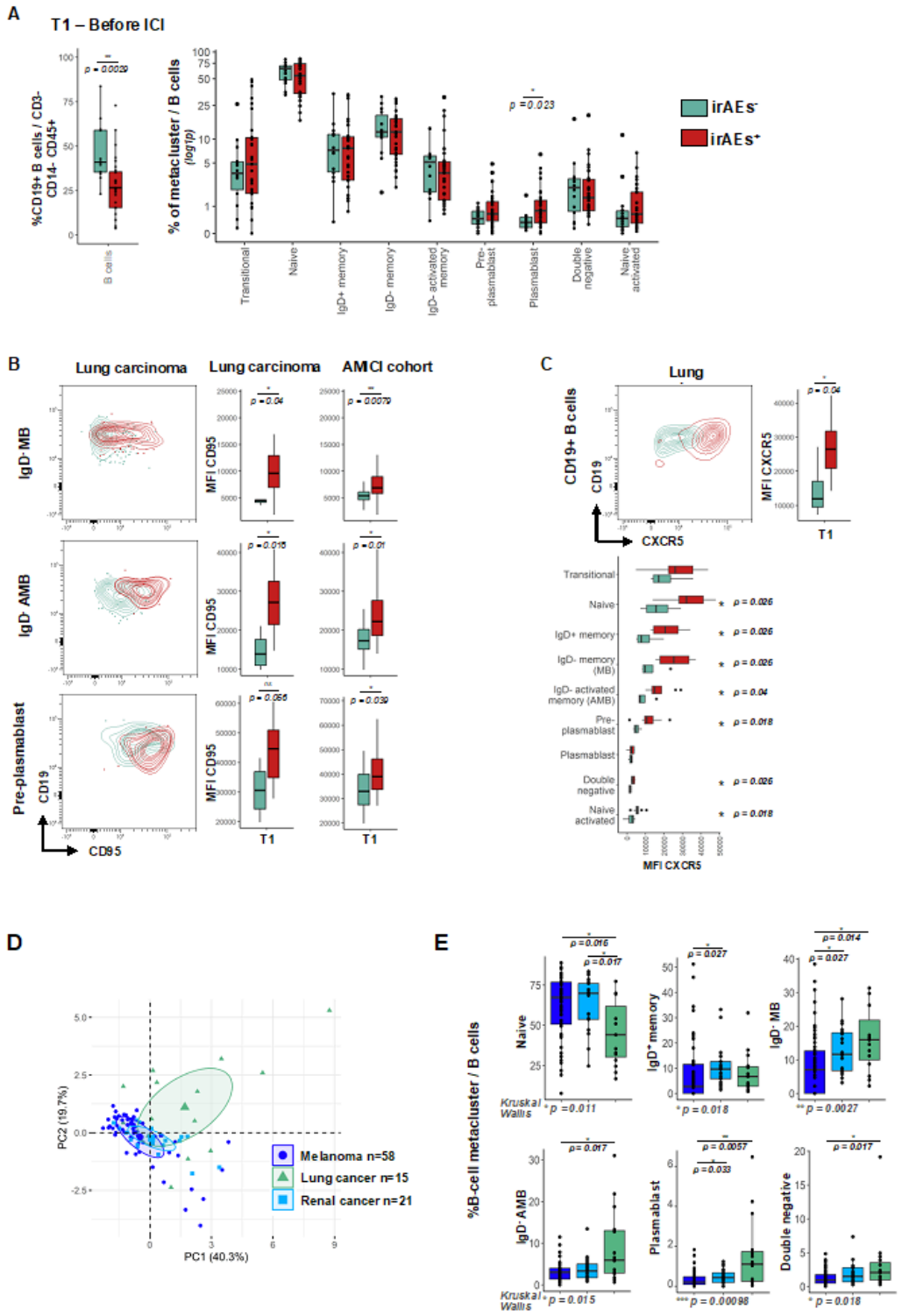


Figure 6

Pan-cancer analysis reveals distinct B-cell activation profiles associated with irAEs. A, Abundance of $CD19^+$ B cells and B-cell metaclusters before ICI (T1) in $irAEs^-$ (n=14) and $irAEs^+$ (n=31) patients from the AMICI pan-cancer cohort. PBMCs were stained with antibody panels 1-5 and analyzed by spectral flow cytometry. Cells were gated as single, live $CD45^+CD3^-CD14^-CD19^+$ B cells. Metaclusters were assigned based on the PRED_1 cohort analysis. **B**, left: Representative dot plots of CD95 and CD19 expression on

IgD$^-$ MB, IgD$^-$ AMB and pre-plasmablasts from irAEs$^-$ (green) and irAEs$^+$ (red) lung carcinoma patients. Right: MFI of CD95 on these subsets is shown for lung carcinoma patients (n=4 irAEs$^-$; n=11 irAEs$^+$) and for all AMICI patients. **C**, Representative CXCR5/CD19 dot plots and CXCR5 MFI on CD19$^+$ B cells and B-cell metaclusters from irAEs$^-$ (green) and irAEs$^+$ (red) lung carcinoma patients. Statistical analyses (summarized in Supplementary Table 13) were performed using Mann-Whitney-Wilcoxon tests; p-values are shown. **D,** Principal component analysis (PCA) of B-cell metacluster abundance colored by cancer type (n=58 melanoma, dark blue; n=15 lung cancer, green; n=21 renal cancer, light blue). **E**, Box plots of B-cell metacluster abundance across melanoma, renal cancer and lung cancer patients. P-values derive from Kruskal-Wallis tests with post hoc Bonferroni-corrected Wilcoxon rank-sum tests. Panels D-E integrate B-cell metacluster data from three cohorts (PRED_1, PRED_2 and AMICI).

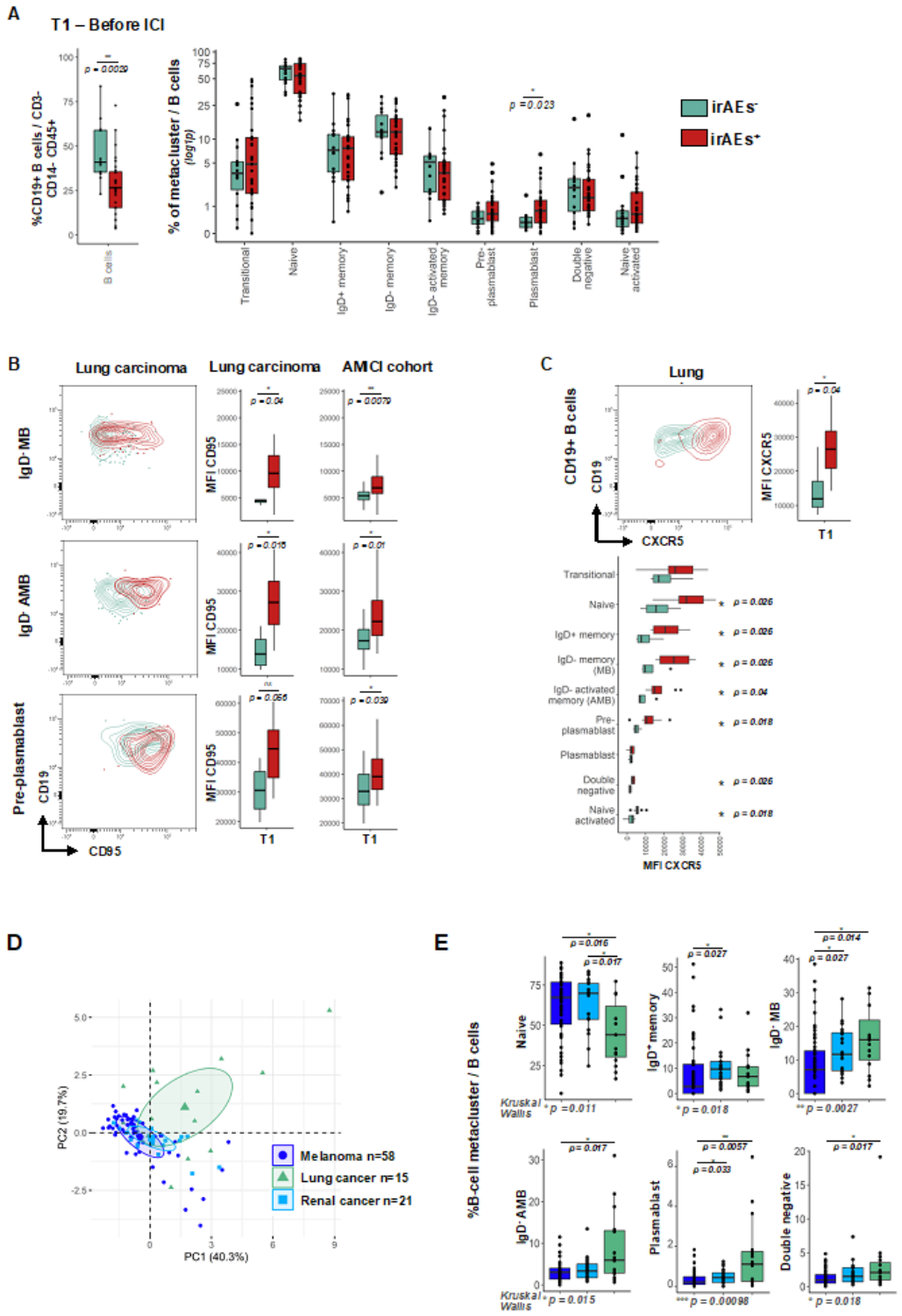


Figure 6

Pan-cancer analysis reveals distinct B-cell activation profiles associated with irAEs. A, Abundance of $CD19^+$ B cells and B-cell metaclusters before ICI (T1) in $irAEs^-$ (n=14) and $irAEs^+$ (n=31) patients from the AMICI pan-cancer cohort. PBMCs were stained with antibody panels 1-5 and analyzed by spectral flow cytometry. Cells were gated as single, live $CD45^+CD3^-CD14^-CD19^+$ B cells. Metaclusters were assigned based on the PRED_1 cohort analysis. **B**, left: Representative dot plots of CD95 and CD19 expression on

IgD$^-$ MB, IgD$^-$ AMB and pre-plasmablasts from irAEs$^-$ (green) and irAEs$^+$ (red) lung carcinoma patients. Right: MFI of CD95 on these subsets is shown for lung carcinoma patients (n=4 irAEs$^-$; n=11 irAEs$^+$) and for all AMICI patients. **C**, Representative CXCR5/CD19 dot plots and CXCR5 MFI on CD19$^+$ B cells and B-cell metaclusters from irAEs$^-$ (green) and irAEs$^+$ (red) lung carcinoma patients. Statistical analyses (summarized in Supplementary Table 13) were performed using Mann-Whitney-Wilcoxon tests; p-values are shown. **D,** Principal component analysis (PCA) of B-cell metacluster abundance colored by cancer type (n=58 melanoma, dark blue; n=15 lung cancer, green; n=21 renal cancer, light blue). **E**, Box plots of B-cell metacluster abundance across melanoma, renal cancer and lung cancer patients. P-values derive from Kruskal-Wallis tests with post hoc Bonferroni-corrected Wilcoxon rank-sum tests. Panels D-E integrate B-cell metacluster data from three cohorts (PRED_1, PRED_2 and AMICI).

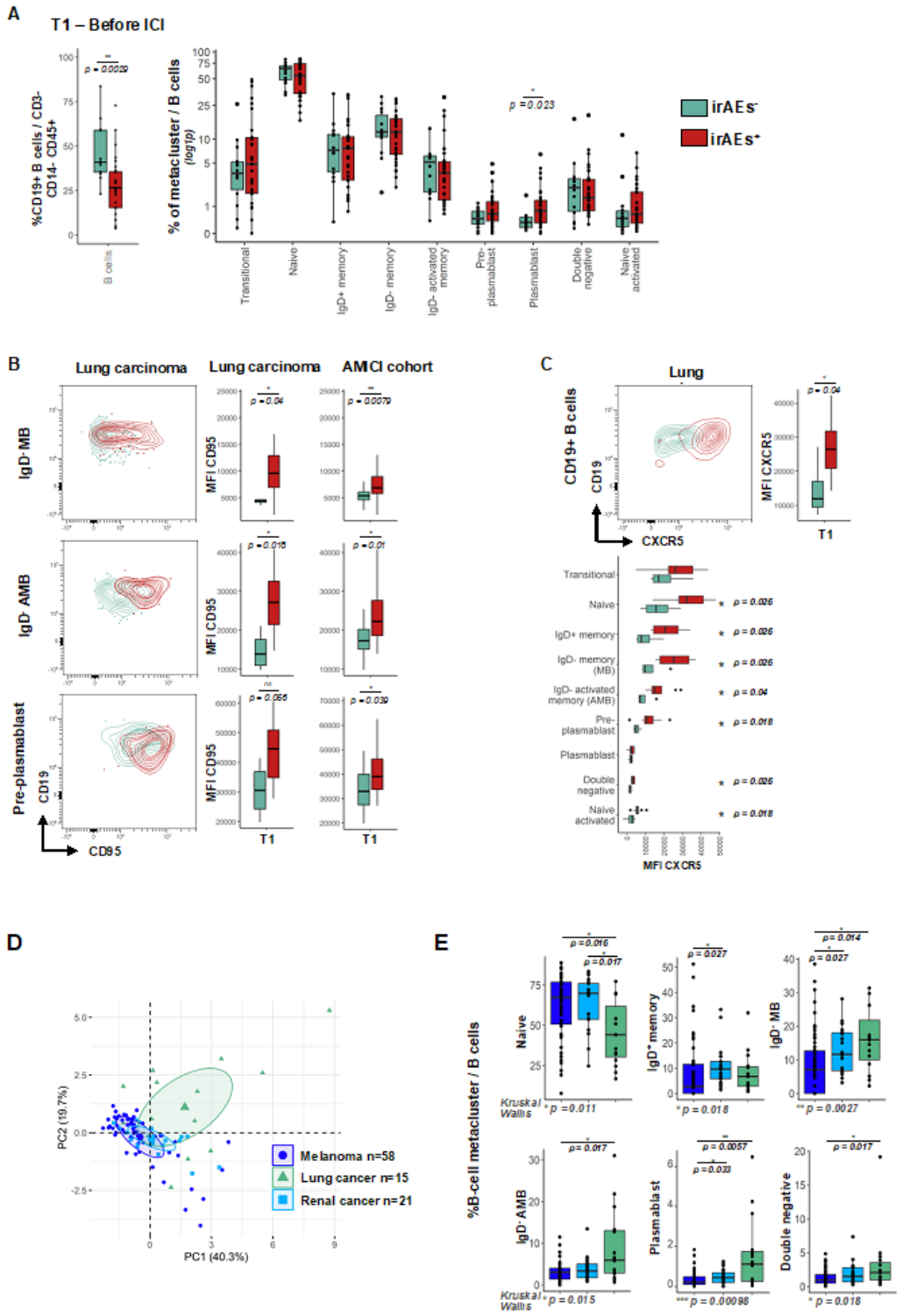


Figure 6

Pan-cancer analysis reveals distinct B-cell activation profiles associated with irAEs. A, Abundance of $CD19^+$ B cells and B-cell metaclusters before ICI (T1) in $irAEs^-$ (n=14) and $irAEs^+$ (n=31) patients from the AMICI pan-cancer cohort. PBMCs were stained with antibody panels 1-5 and analyzed by spectral flow cytometry. Cells were gated as single, live $CD45^+CD3^-CD14^-CD19^+$ B cells. Metaclusters were assigned based on the PRED_1 cohort analysis. **B**, left: Representative dot plots of CD95 and CD19 expression on

IgD$^-$ MB, IgD$^-$ AMB and pre-plasmablasts from irAEs$^-$ (green) and irAEs$^+$ (red) lung carcinoma patients. Right: MFI of CD95 on these subsets is shown for lung carcinoma patients (n=4 irAEs$^-$; n=11 irAEs$^+$) and for all AMICI patients. **C**, Representative CXCR5/CD19 dot plots and CXCR5 MFI on CD19$^+$ B cells and B-cell metaclusters from irAEs$^-$ (green) and irAEs$^+$ (red) lung carcinoma patients. Statistical analyses (summarized in Supplementary Table 13) were performed using Mann-Whitney-Wilcoxon tests; p-values are shown. **D,** Principal component analysis (PCA) of B-cell metacluster abundance colored by cancer type (n=58 melanoma, dark blue; n=15 lung cancer, green; n=21 renal cancer, light blue). **E**, Box plots of B-cell metacluster abundance across melanoma, renal cancer and lung cancer patients. P-values derive from Kruskal-Wallis tests with post hoc Bonferroni-corrected Wilcoxon rank-sum tests. Panels D-E integrate B-cell metacluster data from three cohorts (PRED_1, PRED_2 and AMICI).

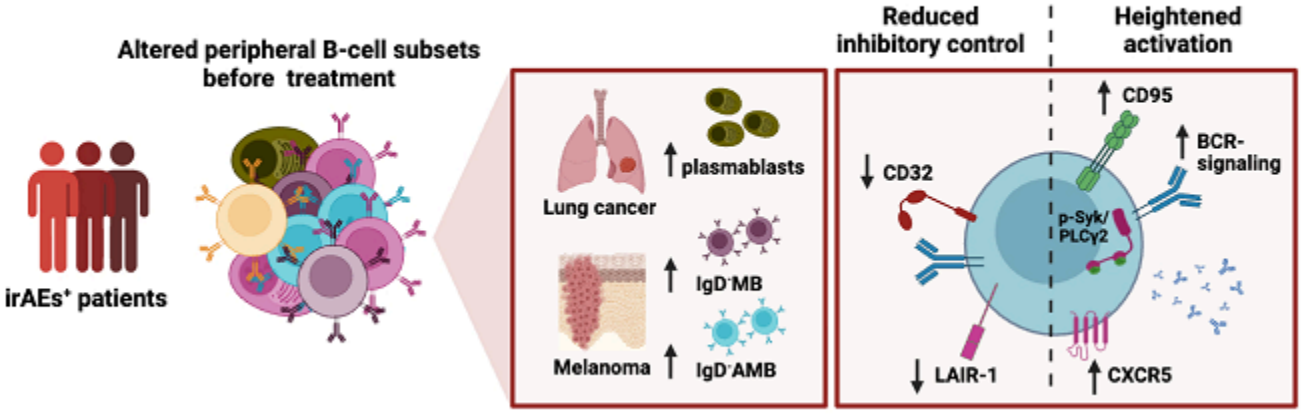


Figure 7

Graphical summary of the main results. Immune checkpoint inhibitors (ICI) targeting CTLA-4 or PD-1 can induce immune-related adverse events [irAEs]. Across two independent cohorts (PREDIMEL and AMICI), patients who subsequently developed irAEs displayed, prior to treatment initiation, an enrichment of highly activated and differentiated B-cell subsets, including plasmablasts in lung cancer and IgD$^-$ memory (MB) and activated memory (AMB) B cells in melanoma. At baseline, B cells from irAEs$^+$ patients exhibited features of reduced inhibitory control, characterized by decreased expression of CD32 and LAIR-1 (PREDIMEL cohort), together with increased expression of activation markers such as CD95 (AMICI cohort). In melanoma, these alterations were associated with enhanced BCR signaling, as evidenced by increased phosphorylation of Syk and PLCγ2, and with increased antibody production upon stimulation, notably IgG secretion by IgD$^-$ memory B cells. These findings support the existence of a pre-existing B-cell immune state poised for activation in patients prone to develop irAEs. Upon ICI treatment, this primed B-cell compartment may synergize with reinvigorated T cells, contributing not only through antibody production but also via antigen presentation and sustained T-cell activation. Consistent with this model, increased CXCR5 expression across multiple B-cell subsets in lung cancer patients

suggests engagement of the CXCL13–CXCR5 axis and tertiary lymphoid structure–associated programs. *Created with Biorender.com*

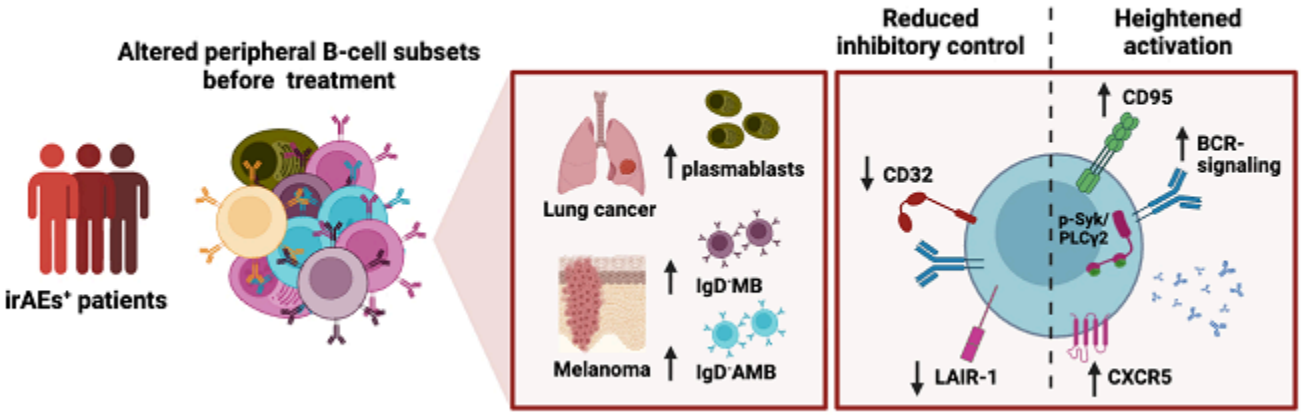


Figure 7

Graphical summary of the main results. Immune checkpoint inhibitors (ICI) targeting CTLA-4 or PD-1 can induce immune-related adverse events [irAEs]. Across two independent cohorts (PREDIMEL and AMICI), patients who subsequently developed irAEs displayed, prior to treatment initiation, an enrichment of highly activated and differentiated B-cell subsets, including plasmablasts in lung cancer and IgD⁻ memory (MB) and activated memory (AMB) B cells in melanoma. At baseline, B cells from irAEs⁺ patients exhibited features of reduced inhibitory control, characterized by decreased expression of CD32 and LAIR-1 (PREDIMEL cohort), together with increased expression of activation markers such as CD95 (AMICI cohort). In melanoma, these alterations were associated with enhanced BCR signaling, as evidenced by increased phosphorylation of Syk and PLCγ2, and with increased antibody production upon stimulation, notably IgG secretion by IgD⁻ memory B cells. These findings support the existence of a pre-existing B-cell immune state poised for activation in patients prone to develop irAEs. Upon ICI treatment, this primed B-cell compartment may synergize with reinvigorated T cells, contributing not only through antibody production but also via antigen presentation and sustained T-cell activation. Consistent with this model, increased CXCR5 expression across multiple B-cell subsets in lung cancer patients suggests engagement of the CXCL13–CXCR5 axis and tertiary lymphoid structure–associated programs. *Created with Biorender.com*

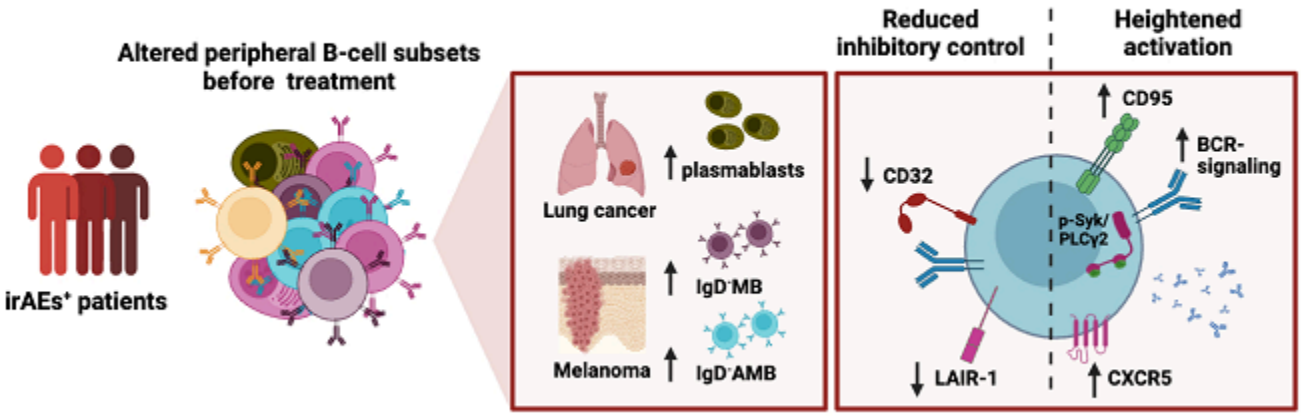


Figure 7

Graphical summary of the main results. Immune checkpoint inhibitors (ICI) targeting CTLA-4 or PD-1 can induce immune-related adverse events [irAEs]. Across two independent cohorts (PREDIMEL and AMICI), patients who subsequently developed irAEs displayed, prior to treatment initiation, an enrichment of highly activated and differentiated B-cell subsets, including plasmablasts in lung cancer and IgD⁻ memory (MB) and activated memory (AMB) B cells in melanoma. At baseline, B cells from irAEs⁺ patients exhibited features of reduced inhibitory control, characterized by decreased expression of CD32 and LAIR-1 (PREDIMEL cohort), together with increased expression of activation markers such as CD95 (AMICI cohort). In melanoma, these alterations were associated with enhanced BCR signaling, as evidenced by increased phosphorylation of Syk and PLCγ2, and with increased antibody production upon stimulation, notably IgG secretion by IgD⁻ memory B cells. These findings support the existence of a pre-existing B-cell immune state poised for activation in patients prone to develop irAEs. Upon ICI treatment, this primed B-cell compartment may synergize with reinvigorated T cells, contributing not only through antibody production but also via antigen presentation and sustained T-cell activation. Consistent with this model, increased CXCR5 expression across multiple B-cell subsets in lung cancer patients suggests engagement of the CXCL13–CXCR5 axis and tertiary lymphoid structure–associated programs. *Created with Biorender.com*

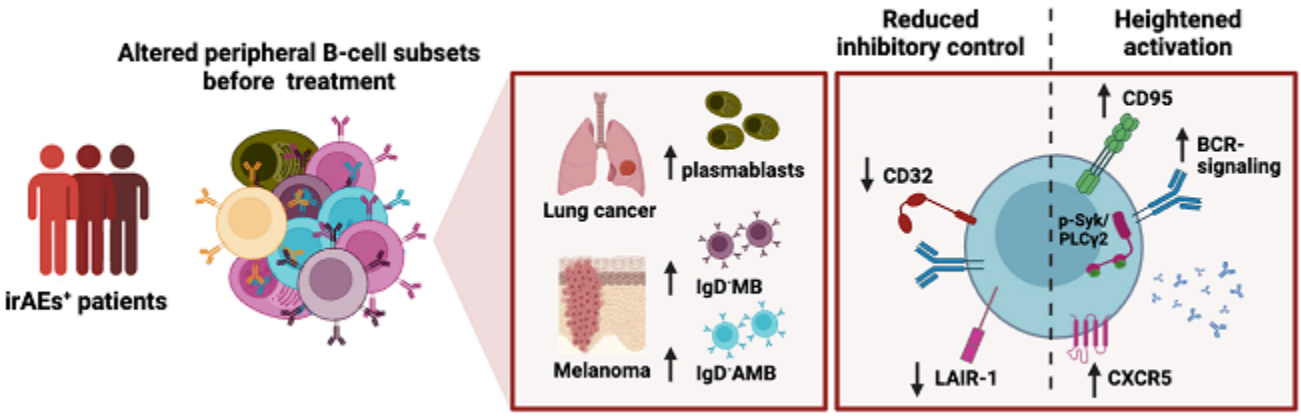


Figure 7

Graphical summary of the main results. Immune checkpoint inhibitors (ICI) targeting CTLA-4 or PD-1 can induce immune-related adverse events [irAEs]. Across two independent cohorts (PREDIMEL and AMICI), patients who subsequently developed irAEs displayed, prior to treatment initiation, an enrichment of highly activated and differentiated B-cell subsets, including plasmablasts in lung cancer and IgD⁻ memory (MB) and activated memory (AMB) B cells in melanoma. At baseline, B cells from irAEs⁺ patients exhibited features of reduced inhibitory control, characterized by decreased expression of CD32 and LAIR-1 (PREDIMEL cohort), together with increased expression of activation markers such as CD95 (AMICI cohort). In melanoma, these alterations were associated with enhanced BCR signaling, as evidenced by increased phosphorylation of Syk and PLCγ2, and with increased antibody production upon stimulation, notably IgG secretion by IgD⁻ memory B cells. These findings support the existence of a pre-existing B-cell immune state poised for activation in patients prone to develop irAEs. Upon ICI treatment, this primed B-cell compartment may synergize with reinvigorated T cells, contributing not only through antibody production but also via antigen presentation and sustained T-cell activation. Consistent with this model, increased CXCR5 expression across multiple B-cell subsets in lung cancer patients suggests engagement of the CXCL13–CXCR5 axis and tertiary lymphoid structure–associated programs. *Created with Biorender.com*

Supplementary Files

This is a list of supplementary files associated with this preprint. Click to download.

- SoussanCancerImmunolImmunotherSupplementaldata.docx
- SoussanCancerImmunolImmunotherSupplementaldata.docx
- SoussanCancerImmunolImmunotherSupplementaldata.docx
- SoussanCancerImmunolImmunotherSupplementaldata.docx